Dynamical investigation of a multirhythmic vibroimpact self-sustained system with enhanced memory damping regime according to correlated noise excitation

R. Mbakob Yonkeu,[1,*] Norbert Marwan,[2] E. N. Francoise,[3] R. Yamapi,[4] and Jurgen Kurths[2,5]

[1]*Department of Physics, Fundamental Physics Laboratory, University of Bamenda, Faculty of Science, P.O. Box 39, Bambili, NWR, Cameroon*

[2]*Potsdam Institute for Climate Impact Research (PIK), Member of the Leibniz Association, Telegraphenberg, P.O. Box 601203, 14473 Potsdam, Germany*

[3]*Department of Physics, University of Yaounde I, P.O. Box 812, Yaounde, Cameroon*

[4]*Department of Physics, Fundamental Physics Laboratory, Faculty of Science, University of Douala, Box 24 157, Douala, Cameroon*

[5]*Department of Physics, Humboldt University, 12 489 Berlin, Germany*

(Received 14 February 2026; revised 31 August 2026; accepted 7 October 2026; published 12 November 2026)

Investigating the dynamics of vibroimpact self-sustaining systems is of immense scientific interest, because systems that undergo vibroimpact interactions can be found in various engineering contexts. Repercussions and associated noise are prevalent in mechanical engineering. Conversely, in a self-sustaining system including viscoelastic material, the damping component is influenced not only by the current time and position, but also by previous states. The memory property of viscoelastic materials is determined by an exponential relaxation function and noise. Based on this viewpoint, this study investigates a self-sustained birhythmic vibroimpact oscillator with improved memory damping subjected to correlated noise. In the beginning, the nonsmooth transformation is implemented to eliminate the discontinuity in the vibroimpact oscillator. The detailed feature space analysis reveals that the correlation time and vibroimpact coefficient can effectively control the oscillator's rhythmic characteristics. To identify the maximal birhythmic zone in parameter space, select an approximate restitution coefficient and correlated noise intensity. In a stochastic environment, decreased noise intensity reduces the essential quantity of the vibroimpact coefficient and control parameters required for birhythmicity. The Rayleigh oscillator is a traditional nonlinear dynamics paradigm, and varying the nonlinear Rayleigh parameters together with vibroimpact coefficients enables control of the nonlinear dynamic multirhythmic system. The reported results demonstrate how the strength of correlated noise, correlation time, restitution coefficient, and system characteristics influence the transition from one potential well to another, and Monte Carlo simulation is used to confirm the stochastic generalized method's effectiveness. Furthermore, for this self-sustaining system, the method of recurrence plots is employed for numerical time series analysis, and the impacts of the restitution coefficient and noise correlation time on recurrence quantification have been demonstrated.

DOI: 10.1103/xfdr-m6j4

I. INTRODUCTION

External disturbances can cause nonlinear behavior in engineering systems, such as chattering, impacts, and collisions [1]. Engineering practice frequently involves impacts, which are necessary for some applications but avoided in others [1–4]. For example, while the interaction of various structural components is required for some processes, such as riveting and hammering, the contact between rotor and stator is problematic. Impacts are a commonly studied topic in mechanics and applied mathematics [3–7]. The impact's nature should be taken into account when choosing the model formulation. A birhythmic system is a nonlinear dynamical system that supports two distinct, coexisting stable oscillatory states under the same set of parameters. Birhythmic systems give efficient and valid models of a wide range of vibrating systems that occur when their components hit with stiff impediments or with one another. There are two approaches for modeling impact effects: the classical impact model [5] and the Hertzian contact model [6–9]. The classical impact model, which is often used in dynamical systems, considers the impact event to be instantaneous by approximation, and the rebound velocity after the instantaneous event is generally smaller in magnitude. Furthermore, the Hertzian contact model provides solutions to systems' behavior that cannot be found by the traditional impact model. However, it can only handle fully elastic impact and is not relevant for scenarios when inelastic impact is present [11]. Multirhythmic systems are common in biological and engineering applications, especially in mechanisms with inflexible impediments, clearances, or gaps [10]. It is of general interest to explore the dynamic behaviors of vibroimpact systems because of their importance in machine and device optimization design, noise suppression, and reliability testing. Vibroimpact systems differ from standard vibrating systems in that they involve impact contact, resulting

*Contact author: raoulmbakob@yahoo.com

Published by the American Physical Society under the terms of the Creative Commons Attribution 4.0 International license. Further distribution of this work must maintain attribution to the author(s) and the published article's title, journal citation, and DOI.

in nonsmooth, nonlinear effects that require extensive modeling and processing.

To perform numerical simulations of impact vibrations in a nonlinear dynamical system such as the one employed in this research, standard ordinary differential equation solvers are typically utilized in conjunction with event-handling subroutines. Smoothed discontinuities in impact force models can be used directly with typical ordinary differential equation solvers [12–14]. Nonlinear dynamics can be studied using a wide range of mathematical techniques and methodologies [13]. Noise can affect oscillatory motion [15,16], leading to transitions comparable to those between stable points [17]. There is a significant body of literature on friction stochastic multirhythmic systems and vibroimpact stochastic systems. Many analytical approaches for smooth stochastic multirhythmic systems, such as stochastic averaging and path integration, become useless due to velocity jumps [11,18]. Wang *et al.* [18] studied the critical transition problem for a stochastically forced birhythmic vibroimpact model with improved memory damping regime effect. Ivanov [19] proposed a nonsmooth coordinate; in [20–24], the writers used an approximate method called stochastic averaging to study the response and bifurcation of vibroimpact multirhythmic systems. Zhu [25] employed the exponential-polynomial closure approach to investigate the stochastic response of a vibroimpact system driven by external Poisson noise excitations. Vibroimpact events are common in mechanical engineering, often resulting in noise, wear, and complex dynamic responses. To capture these phenomena, vibroimpact self-sustaining systems have been widely researched as nonlinear models with practical applications. Within nonlinear dynamics, the Rayleigh oscillator is a standard model for investigating oscillatory regimes. Birhythmic systems, which have two distinct stable oscillatory states, are particularly interesting, as are multirhythmic dynamics, in which many rhythms coexist. These multirhythmic reactions can be regulated and controlled by altering the nonlinear Rayleigh parameters as well as the vibroimpact coefficients. This work looks into how such parameter variations affect the dynamics of vibroimpact self-sustaining systems, perhaps revealing new insights into their controllability and engineering applications. Previous studies on friction-damped and vibroimpact stochastic systems have mostly focused on bifurcation. Inspired by these points of view, this paper explores the significance of noise parameter values, vibroimpact coefficients, and nonlinear parameters on escape time, residence time, mean first passage time, time series, recurrence plot measurements, and so on in the vibroimpact stochastic Rayleigh systems with memory damping. The remainder of the article is structured in the following manner. Section II provides an explanation of the system and its simplification. Section III describes the near-stationary solutions. Section IV provides an example to demonstrate the usefulness of the proposed strategy and discusses stochastic bifurcation. Finally, Sec. V contains our conclusions.

II. ANALYTICAL ESTIMATES FOR THE PROPOSED SELF-SUSTAINED VIBROIMPACT MODEL

A. Definition of the self-sustained model

We studied the following version of a generalized Rayleigh oscillator to add better memory damping, a typical nonsmooth condition (vibroimpact constraint), and a random contribution to the oscillator. The system is regulated by the equations

$$\begin{aligned} &\ddot{x} + \omega_0^2 x + Z(x,\dot{x}) = \mu(c_1 - c_2\dot{x}^2 + \alpha\dot{x}^4 - \beta\dot{x}^6)\dot{x} + \mu^{1/2} f(t), \quad x > \Delta, \\ &\dot{x}_p = -r\dot{x}_n, \quad x = \Delta, \end{aligned} \tag{1}$$

where x is the displacement state variable, and its overdots stand for differentiation with respect to time t, which form velocity and acceleration state variables of the oscillator. ω_0 represents the linear undamped natural frequency of the oscillator. α, β are the nonlinear control parameters that determine the amplitude and stability of oscillations, c_1 and c_2 tune the Rayleigh damping coefficients, controlling nonlinear energy dissipation damping, and μ modulates the nonlinearity of damping. The birhythmic oscillator, which combines modifying parameters (primarily α and β) with a displacement state variable, is suitable for modeling several biological processes. Improved memory or viscoelastic damping $Z(x,\dot{x})$ encompasses both the historical and current stages of motion, based on the viscoelastic property of the material. The constitutive calculation model is chosen as $Z(x(t),\dot{x}(t)) = \int_0^t \rho(t-t')[h\dot{x}(t') + gx(t')]dt'$, where h and g reflect the velocity and displacement feedback gains, respectively. $\rho(t)$ is the relaxation function defined as $\rho(t) = \zeta \exp(\frac{-t}{\lambda})$, where λ is the relaxation time with a non-negative value, and ζ denotes its magnitude, which can be either positive or negative. $f(t)$ represents the Gaussian correlated noise, whose statistical features can be characterized as $< f(t) >= 0$, $< f(t)f(t-t') >= \frac{D}{\tau}\exp(\frac{-|t-t'|}{\tau})$, where D and τ are the correlated noise intensity and correlation time, respectively. The second equation of Eq. (1) defining the vibroimpact constraint is composed of four elements: the position of rigid wall Δ; the subscripts $\dot{x}_n$ and $\dot{x}_p$ refer to the velocities of the system preceding and following, respectively, the instant t_Δ of impacts r, with $0 < r \leqslant 1$ illustrating the degree of energy loss when impact occurs and is known as the restitution coefficient.

B. Nonsmooth transformation

To convert the vibroimpact constraint, a mirror image transformation must be used in conjunction with this unilateral constraint. The nonsmooth transformation is proposed as follows:

$$\begin{aligned} &x = x_1 = |V| = V\,\mathrm{sgn}(V), \quad \dot{x} = x_2 = \dot{V}\,\mathrm{sgn}(V), \\ &\ddot{x} = x_3 = \ddot{V}\,\mathrm{sgn}(V), \end{aligned} \tag{2}$$

where $\mathrm{sgn}(V)$ is the signum function of V, such that

$$\mathrm{sgn}(V) = \begin{cases} -1 & \text{if } V < 0, \\ 0 & \text{if } V = 0, \\ +1 & \text{if } V > 0. \end{cases}$$

Obviously, the transformation Eq. (2) maps the domain $x > 0$ of the original phase plane $(x, \dot{x})$ onto the whole phase plane $(V, \dot{V})$, and makes the transformed velocity $\dot{V}$ continuous when $r = 1$. Substituting Eq. (2) into Eq. (1), the equations of the new variables can be written as follows:

$$\begin{aligned} &\ddot{V} + \omega_0^2 V + \mathrm{sgn}(V) Z[\mathrm{sgn}(V)V + \Delta, \mathrm{sgn}(V)\dot{V}] = \mu(c_1 - c_2\dot{V}^2 + \alpha\dot{V}^4 - \beta\dot{V}^6)\dot{V} + \mu^{1/2}\mathrm{sgn}(V) f(t) - \Delta\omega_0^2 \mathrm{sgn}(V), \quad t \neq t_\Delta, \\ &\dot{V}_p = r\dot{V}_n, \quad t = t_\Delta. \end{aligned} \tag{3}$$

Here, the second equation of Eq. (3) is a constraint equation. Clearly, at $t = t_\Delta$, there is a discontinuity in the velocity due to the impact when $r \neq 1$. The change in the velocity when $y(t_\Delta) = 0$ (at impact) is given by

$$(\dot{V}_n - \dot{V}_p)\delta(t - t_\Delta) = (1 - r)\dot{V}\delta(t - t_\Delta), \tag{4}$$

provided $|\dot{V}_p| < |\dot{V}| < |\dot{V}_n|$. Since $V(t) \approx V(t_\Delta) + \dot{V}(t)(t - t_\Delta)$ in a small time interval after impact and $V(t_\Delta) = 0$, it follows that one can approximate

$$\delta(t - t_\Delta) \approx |\dot{V}(t)|\delta(V). \tag{5}$$

Here, the function $\delta(.)$ must be interpreted as some distribution function such that when applied to a smooth enough function $\phi(t)$, one gets $\int_{-\infty}^{\infty} \phi(s)\delta(s - t)ds = \phi(t^-)$. In other words, the function $\delta(.)$ implies that the velocity is approximated to be just prior to the impact. Note that the conventional interpretation of $\delta(.)$ as a Dirac-delta function implies that $\delta(.)$ takes the value exactly at $t = t_\Delta$ and would lead to difficulties, as there would be a discontinuous factor $\dot{V}|\dot{V}|$ at $V = 0$. The transformation in Eq. (5) leads to modeling the effect of impact as a dissipation term, given by the approximation

$$(1 - r)\dot{V}\delta(t - t_\Delta) \approx (1 - r)\dot{V}|\dot{V}|\delta(V), \tag{6}$$

given that $|\dot{V}_p| < |\dot{V}| < |\dot{V}_n|$. This transformation allows 'ignoring' the impact condition. Because of the velocity discontinuity, the impulsive damping can be interpreted to occur shortly before the velocity leap, and it is justified when $(1 - r)$ is small, i.e., when the coefficient of restitution is close to unity. Equations (4)–(6) contain more considerations on the distribution-based interpretation of differential operations with nonsmooth functions. Equations (3)–(6) can be combined into a single equation of motion in the form

$$\begin{aligned} \ddot{V} + \omega_0^2 V + \mathrm{sgn}(V) Z[\mathrm{sgn}(V)V + \Delta, \mathrm{sgn}(V)\dot{V}] = {} & \mu(c_1 - c_2\dot{V}^2 + \alpha\dot{V}^4 - \beta\dot{V}^6)\dot{V} + \mu^{1/2}\mathrm{sgn}(V) f(t) \\ & - (1 - r)\dot{V}|\dot{V}|\delta(V) - \Delta\omega_0^2 \mathrm{sgn}(V). \end{aligned} \tag{7}$$

C. Stochastic averaging approach

For tiny VI losses, random disturbances, and mild damping, Eq. (7) can be approached as a quasiconservative system with the answer that follows:

$$\begin{aligned} V_1 = V(t) &= A(t)\cos\phi(t), \\ V_2 = \dot{V}(t) &= -A(t)\tilde{\omega}\sin\phi(t), \\ \phi(t) &= \tilde{\omega}t + \theta, \end{aligned} \tag{8}$$

with A, ϕ, and θ being random processes. Therefore, the IMDR term can be calculated with small delay t' (see the Appendix for more explanation),

$$\begin{aligned} \mathrm{sgn}(V_1) Z[\mathrm{sgn}(V_1)V_1 + \Delta, \mathrm{sgn}(V_1)V_2] = {} & \lambda(\tilde{\omega}^2\lambda^2 + 1)^{-1}\zeta([e^{-t/\lambda}(\tilde{\omega}\lambda\sin(\tilde{\omega}t) - \cos(\tilde{\omega}t) + \Lambda_1(\Delta)) + 1]gV_1 \\ & + [\lambda\tilde{\omega}^2 - e^{-t/\lambda}(\tilde{\omega}\sin(\tilde{\omega}t) + \lambda\tilde{\omega}^2\cos(\tilde{\omega}t))]hV_1 \\ & + [1 - e^{-t/\lambda}(\cos(\tilde{\omega}t) - \lambda\tilde{\omega}\sin(\tilde{\omega}t))]hV_2 \\ & + [e^{-t/\lambda}(\lambda\cos(\tilde{\omega}t) + \tilde{\omega}^{-1}\sin(\tilde{\omega}t) + \Lambda_2(\Delta)) - \lambda]gV_2), \end{aligned} \tag{9}$$

in which $\Lambda_1(\Delta)$, $\Lambda_2(\Delta)$ denote the bounded functions of the VI constraint. As the system is confronted with excitations for a long time period, enhanced memory mechanism control adds to damping and stiffness, which is commensurate with the physical properties of viscoelastic materials [Eq. (9)]. The system equation has been shortened to

$$\begin{aligned} \dot{V}_2 + \tilde{\omega}^2 V_1 + \Delta\omega_0^2 \mathrm{sgn}(V_1) = {} & \mu[c_1 - c_2 V_2^2 + \alpha V_2^4 - \beta V_2^6 + \mu^{-1}\lambda^2(\tilde{\omega}^2\lambda^2 + 1)^{-1} g\zeta - \mu^{-1} h\lambda\zeta(\tilde{\omega}^2\lambda^2 + 1)^{-1} \\ & - \mu^{-1}(1 - r)|V_2|\delta(V_1)]V_2 + \mu^{1/2}\mathrm{sgn}(V_1) f(t), \end{aligned} \tag{10}$$

where $\tilde{\omega}^2 = \lambda(\tilde{\omega}^2\lambda^2+1)^{-1}[h\zeta\lambda\tilde{\omega}^2+\zeta g]+\omega_0^2$. Setting Δ to the origin of unilateral constraint, potential energy $E_p(V_1)$ and total energy E of the converted system are expressed as

$$E_p(V_1) = \int_0^{V_1} \tilde{\omega}^2 x dx = \frac{1}{2}\tilde{\omega}^2 V_1^2, \quad E = E_p(V_1) + \frac{1}{2}V_2^2. \tag{11}$$

Based on this, one can obtain the equations for the amplitude A and the phase angle θ from Eq. (10) as

$$\begin{aligned}
\frac{dA}{dt} &= -\mu\beta A^7\tilde{\omega}^6\sin^8\phi + \mu\alpha A^5\tilde{\omega}^4\sin^6\phi - \mu c_2 A^3\tilde{\omega}^2\sin^4\phi + \mu c_1 A\sin^2\phi + \lambda^2(\tilde{\omega}^2\lambda^2+1)^{-1}g\zeta A\sin^2\phi \\
&\quad -h\lambda\zeta(\tilde{\omega}^2\lambda^2+1)^{-1}A\sin^2\phi - \tilde{\omega}^{-1}\mu^{1/2}\sin\phi\,\mathrm{sgn}(A\cos\phi)f(t), \\
\frac{d\theta}{dt} &= -\mu\beta A^6\tilde{\omega}^6\sin^7\phi\cos\phi + \mu\alpha A^4\tilde{\omega}^4\sin^5\phi\cos\phi - \mu c_2 A^2\tilde{\omega}^2\sin^3\phi\cos\phi + \mu c_1\sin\phi\cos\phi \\
&\quad + \lambda^2(\tilde{\omega}^2\lambda^2+1)^{-1}g\zeta\sin\phi\cos\phi - h\lambda\zeta(\tilde{\omega}^2\lambda^2+1)^{-1}\sin\phi\cos\phi - \tilde{\omega}^{-1}A^{-1}\mu^{1/2}\cos\phi\,\mathrm{sgn}(A\cos\phi)f(t).
\end{aligned} \tag{12}$$

The stochastic averaging method [26] approximates (A,θ) as a two-dimensional random diffusion process, allowing for the mean drift coefficient and mean diffusion coefficient of the Fokker-Planck-Kolmogorov (FPK) equation to be obtained after combining over the time frame of oscillations $(2\pi/\tilde{\omega})$. The Itô equation of the amplitude $A(t)$ can be given,

$$dA = m(A)dt + \sigma(A)dW_1(t), \tag{13}$$

where $W_1(t)$ denotes a normalized Wiener process, and $m(A)$, $\sigma(A)$ represent the mean drift and mean diffusion coefficients, respectively,

$$\begin{aligned}
m(A) &= -\frac{35}{128}\beta\mu\tilde{\omega}^6A^7 + \frac{5}{16}\alpha\mu\tilde{\omega}^4A^5 - \frac{3}{8}c_2\mu\tilde{\omega}^2A^3 + \frac{1}{2}c_1\mu A \\
&\quad + \frac{1}{2}\lambda^2(\tilde{\omega}^2\lambda^2+1)^{-1}g\zeta A - \frac{1}{2}h\lambda\zeta(\tilde{\omega}^2\lambda^2+1)^{-1}A - \tilde{\omega}(1-r)\frac{A}{\pi} + \frac{\mu D}{2A(1+\tau^2)\tilde{\omega}^2}, \\
\sigma^2(A) &= \frac{\mu D}{\tilde{\omega}^2(1+\tau^2)}.
\end{aligned} \tag{14}$$

The Langevin equation (13) of the Brownian motion of the particle in a three-well potential can therefore be approximated by

$$\dot{A} = -\frac{dU(A)}{dA} + \sqrt{\frac{\mu D}{\tilde{\omega}^2}}\dot{W}_1, \quad = G(A) + \sqrt{\frac{\mu D}{\tilde{\omega}^2}}\dot{W}_1, \tag{15}$$

where

$$G(A) = -\frac{dU(A)}{dA}, \tag{16}$$

and the effective pseudopotential $U(A)$ is given by

$$\begin{aligned}
U(A) &= \frac{35}{1024}\beta\mu\tilde{\omega}^6A^8 - \frac{5}{96}\alpha\mu\tilde{\omega}^4A^6 + \frac{3}{32}c_2\mu\tilde{\omega}^2A^4 - \frac{1}{4}c_1\mu A^2 \\
&\quad - \frac{1}{4(\tilde{\omega}^2\lambda^2+1)}(\lambda^2 g\zeta - h\lambda\zeta)A^2 + \tilde{\omega}(1-r)\frac{A^2}{2\pi} - \frac{\mu D ln(A)}{2(1+\tau^2)\tilde{\omega}^2}.
\end{aligned} \tag{17}$$

The stationary oscillating states are achieved for $\partial U(A)/\partial A = 0$, with the associated amplitude equation reading

$$\begin{aligned}
&+ \frac{\mu A}{1024}[-280\beta\tilde{\omega}^6A^6 + 320\alpha\tilde{\omega}^4A^4 - 384c_2\tilde{\omega}^2A^2 + 512c_1] \\
&+ \frac{1}{2(\tilde{\omega}^2\lambda^2+1)}(\lambda^2 g\zeta - h\lambda\zeta)A - \tilde{\omega}(1-r)\frac{A}{\pi} + \frac{\mu D}{2(1+\tau^2)\tilde{\omega}^2A} = 0.
\end{aligned} \tag{18}$$

Along the same line, one can derive the FPK equation for the amplitude in the form

$$\frac{\partial P(A,t)}{\partial t} = -\frac{\partial}{\partial A}[m(A)P(A,t)] + \frac{1}{2}\frac{\partial^2}{\partial A^2}[\sigma^2(A)P(A,t)], \tag{19}$$

Solving Eq. (19), one obtains the stationary probability density function (PDF) for the amplitude in the form

$$\begin{aligned} P(A) &= \frac{N_o}{\sigma^2(A)} \exp\left[\int_0^A \frac{2m(v)}{\sigma^2(v)} dv\right] \\ &= \frac{N_o \tilde{\omega}^2 A(1+\tau^2)}{\mu D} \exp\Bigg[-\frac{35(1+\tau^2)}{512D}\beta\tilde{\omega}^8 A^8 \\ &\quad + \frac{5(1+\tau^2)}{48D}\alpha\tilde{\omega}^6 A^6 - \frac{3(1+\tau^2)}{16D}c_2\tilde{\omega}^4 A^4 + \frac{(1+\tau^2)}{2D}c_1\tilde{\omega}^2 A^2 \\ &\quad + \frac{(1+\tau^2)}{2\mu D(\tilde{\omega}^2\lambda^2+1)}(\tilde{\omega}^2\lambda^2 g\zeta - \tilde{\omega}^2 h\lambda\zeta)A^2 - \tilde{\omega}^3(1-r)\frac{A^2(1+\tau^2)}{\mu\pi D}\Bigg], \end{aligned} \tag{20}$$

where N_o is the normalization constant which satisfies

$$\begin{aligned} N_o = \Bigg[\int_0^\infty \frac{\tilde{\omega}^2 A(1+\tau^2)}{\mu D} \exp\Bigg[&-\frac{35(1+\tau^2)}{512D}\beta\tilde{\omega}^8 A^8 + \frac{5(1+\tau^2)}{48D}\alpha\tilde{\omega}^6 A^6 - \frac{3(1+\tau^2)}{16D}c_2\tilde{\omega}^4 A^4 + \frac{(1+\tau^2)}{2D}c_1\tilde{\omega}^2 A^2 \\ &+ \frac{(1+\tau^2)}{2\mu D(\tilde{\omega}^2\lambda^2+1)}(\tilde{\omega}^2\lambda^2 g\zeta - \tilde{\omega}^2 h\lambda\zeta)A^2 - \tilde{\omega}^3(1-r)\frac{(1+\tau^2)A^2}{\mu\pi D}\Bigg] dA\Bigg]^{-1}. \end{aligned} \tag{21}$$

By executing $\frac{\partial P(A)}{\partial A} = 0$, the extrema A_m of the distribution expression from Eq. (20) are controlled by the positive real roots of the equation,

$$\begin{aligned} \Bigg[1 - \frac{35(1+\tau^2)}{64D}\beta\tilde{\omega}^8 A^8 + \frac{5(1+\tau^2)}{8D}\alpha\tilde{\omega}^6 A^6 - \frac{3(1+\tau^2)}{4D}c_2\tilde{\omega}^4 A^4 + \frac{(1+\tau^2)}{D}c_1\tilde{\omega}^2 A^2 \\ + \frac{(1+\tau^2)}{\mu D(\tilde{\omega}^2\lambda^2+1)}(\tilde{\omega}^2\lambda^2 g\zeta - \tilde{\omega}^2 h\lambda\zeta)A^2 - 2\tilde{\omega}^3(1-r)\frac{(1+\tau^2)A^2}{\mu D\pi}\Bigg] = 0. \end{aligned} \tag{22}$$

Then, the stationary PDF of the total energy $E = E_p(A) = \frac{1}{2}\tilde{\omega}^2 A^2$ can be retrieved so that

$$P(E) = P(A)\left|\frac{dA}{dE}\right| = \left.\frac{P(A)}{\tilde{\omega}^2 A}\right|_{A=E_p^{-1}(E)}. \tag{23}$$

The initial approximation for the combined probability density of displacement and velocity can be determined as follows:

$$\begin{aligned} P(x_1, x_2) = \left.\frac{P(E)}{T(E)}\right|_{E=\frac{1}{2}\tilde{\omega}^2 x_1^2 + \frac{1}{2}x_2^2} &= \frac{K_o\omega_0(1+\tau^2)}{2\pi D} \exp\Bigg[\frac{\mu\omega_0^2(1+\tau^2)}{512D}\Bigg\{256\left(x_1^2 + \frac{x_2^2}{\omega_0^2}\right) \\ &- 32\left(x_1^2 + \frac{x_2^2}{\omega_0^2}\right)^2 + \frac{32}{3}\alpha\left(x_1^2 + \frac{x_2^2}{\omega_0^2}\right)^3 - 5\beta\left(x_1^2 + \frac{x_2^2}{\omega_0^2}\right)^4 \\ &+ \frac{k\omega_0^2(1+\tau^2)}{2D}\omega^{p-1}\sin\left(\frac{p\pi}{2} - \omega\rho\right)\left(x_1^2 + \frac{x_2^2}{\omega_0^2}\right)\Bigg], \end{aligned} \tag{24}$$

with $T(E) = \frac{2\pi}{\tilde{\omega}}$.

III. CRITICAL TRANSITIONS ANALYSIS

Next, we are able to discover the viable transition eventualities of the oscillator consistent with Eq. (1) on the basis of numerical strategies to help in getting rid of limitations on analysis. The consequences of the Rayleigh damping variant, VI constraint, viscoelastic force, and correlated noise at the differences of the SPDF from one shape to any other can be elaborated with the parameter reference value $c_1 = 1.0$, $c_2 = -1.0$, $\omega_0 = 1.0$, $\zeta = -0.01$, $\lambda = 1.0$, $r = 0.95$, $\alpha = 3.0$, $\beta = 1.25$, $D = 0.7$, $h = 0.0$, $g = 1.0$, and $\mu = 0.01$, unless otherwise specified.

A. Birhythmic properties and effect of vibroimpact coefficient on pseudopotential

This section summarizes the dynamical attractors of the birhythmic vibroimpact oscillator with improved memory damping regime and correlated noise excitation. The parameters α and β determine whether the system depicted by Eq. (1) has one or three limit cycles (if three limit cycles are achieved, two are stable and one is unstable). The unstable limit cycle is the separatrix between the basins of attraction of the two stable limit cycles with differing frequencies. In Fig. 1, we show the bifurcation lines that contour the region of

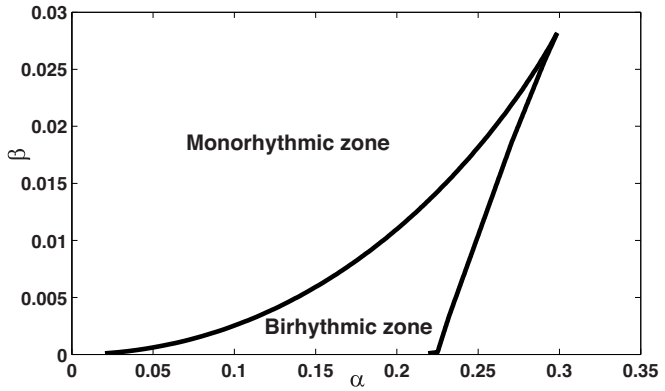


FIG. 1. Domain of existence of three limit cycles in plane (α, β). The parameter values are $c_1 = 1.0$, $c_2 = -1.0$, $\omega_0 = 1.0$, $\zeta = -0.01$, $\lambda = 1.0$, $r = 1.0$, $D = 0.0$, $h = 0.0$, $g = 1.0$, and $\mu = 0.01$.

birhythmicity in the parameter (α, β). In this figure, we present both birhythmic and monorhythmic regions. To analyze the effects of the control parameter on the amplitude response $A(\alpha)$ or $A(\beta)$, we again consider stationary oscillations from the amplitude equation defined in Eq. (18) to derive the resulting amplitude as a function of the control parameter. This is shown in Fig. 2, where there appears a sudden jump: The amplitude response shows multiple limit solutions for low α and β. Figures 2(a) and 2(c) compare numerical simulation (blue lines) with analytical results (black lines) to validate the analytical approach's results. Birhythmicity allows for the change of two stable attractors with clearly different periods (or frequencies) and amplitudes of oscillations by varying the perturbation or control parameters appropriately. Jumps arise when nonlinear damping and control parameters (α, β) change the balance of energy input and dissipation. When damping is weak, the oscillator can maintain two separate rhythms. The unstable branch serves as a threshold dividing basins of attraction, which explains why modest parameter changes cause rapid alterations. The stable and unstable limit-cycle amplitudes are numerically determined using the fourth-order Runge-Kutta method [solving Eq. (1) without noise], as shown in Fig. 3. We plot the velocity as a function of position for different parameters (α, β) of the existence field of three limit cycles. We observe that the system's behavior varies as the parameters change. These figures indicate the struggle between self-sustaining Rayleigh energy input; here, the unstable cycle is the trajectories within it decay to the small-amplitude rhythm, while those outside increase toward the large-amplitude rhythm. Generally, the region of existence of three limit cycles, a condition for birhythmicity, decreases with the increase of the nonlinear parameter; see Fig. 4(a), and increases when the correlation time increases; see Fig. 4(b). We can remark that for this system [Eq. (1)], the value of the control parameter where the birhythmicity is presented can be more than 50; this was not the case for the

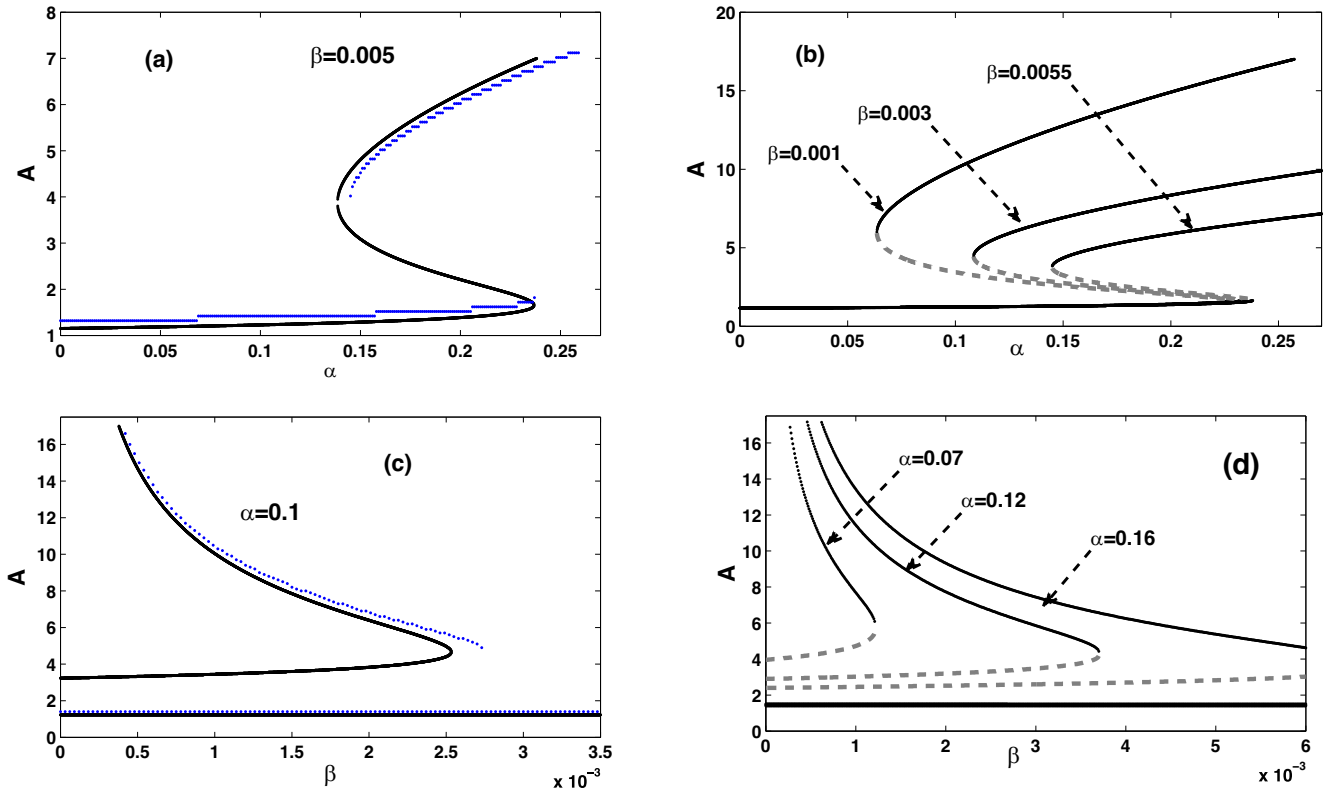


FIG. 2. Amplitude versus control parameter α [(a) and (b)] and β[(c) and (d)]. Corresponding to (b) and (c), the solid line denotes the stable solution, and the dashed line represents the unstable branch. In (a) and (c), the blue lines and the black lines correspond respectively to the numerical results and the analytical result. The other parameter values are: $c_1 = 1.0$, $c_2 = -1.0$, $\omega_0 = 1.0$, $\zeta = -0.01$, $\lambda = 1.0$, $r = 1.0$, $D = 0.0$, $h = 0.0$, $g = 0.0$, and $\mu = 0.001$.

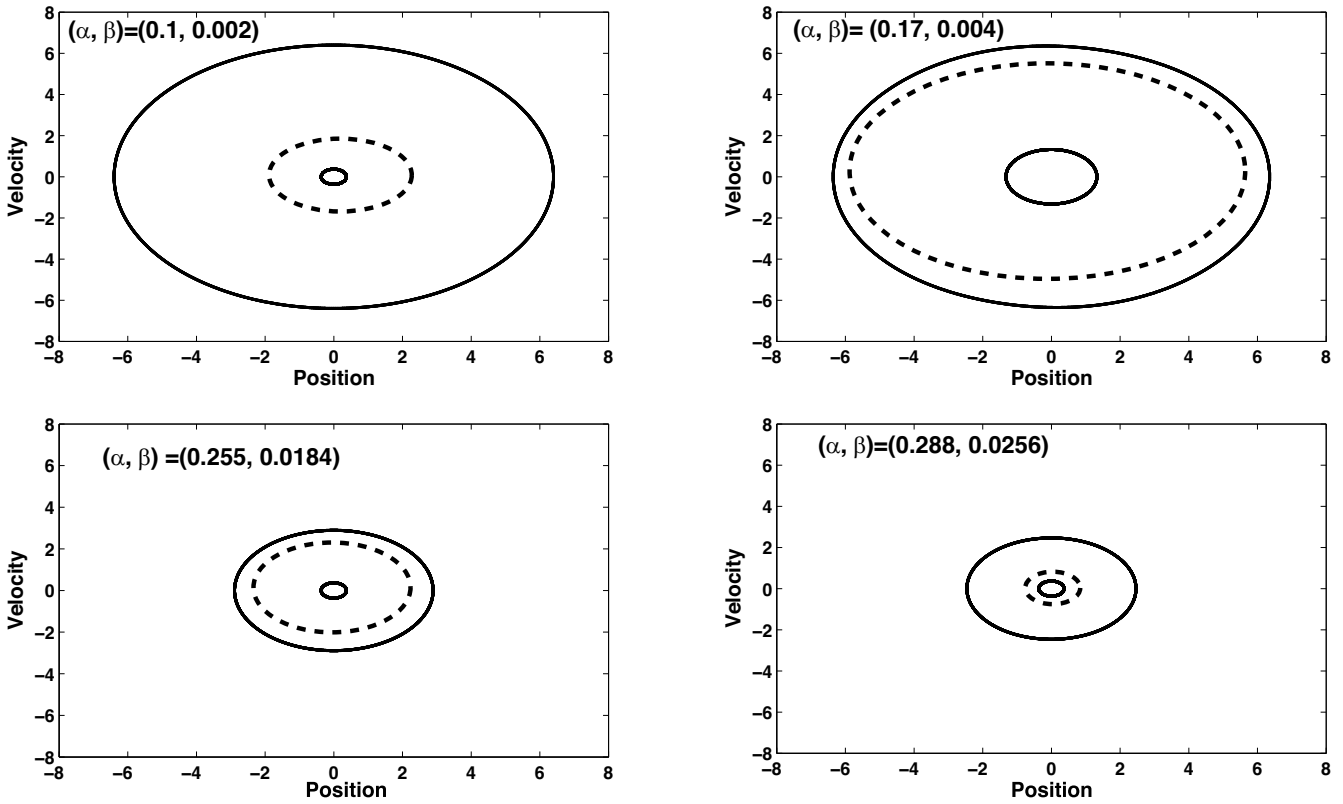


FIG. 3. Corresponding phase space plot showing the location of the stable limit cycles (solid lines) along with the unstable limit cycle (dotted lines) for different control parameters taken in the birhythmic zone when the parameter values are: $c_1 = 1.0$, $c_2 = -1.0$, $\omega_0 = 1.0$, $\zeta = -0.01$, $\lambda = 1.0$, $r = 1.0$, $D = 0.0$, $h = 0.0$, $g = 1.0$, and $\mu = 0.001$.

birhythmic Van der Pol system. Finally, in Fig. 5, we represent the bifurcation diagram for the system parameter plane (r, D) when the control parameter is taken in the birhythmic zone [Fig. 5(a)] and in the monorhythmic zone [Fig. 5(b)]. A higher restitution coefficient results in reduced energy loss at impact, which promotes the coexistence of many rhythms. Noise strength works as a destabilizing factor: little noise maintains birhythmicity, whereas excessive noise pushes escape between wells, reducing the birhythmic region. The effect of (α, β) taken in the monorhythmic region in the domain of (r, D) where the system is birhythmic is shown, and we can conclude that the coupling of noise and the vibroimpact system can reduce the monorhyhmicity to a birhythmicity. This occurs, see Fig. 5, for high values of the parameter r and D, close to the disappearance of the birhythmic region. We display in Figs. 6 and 7 the variation of the pseudopotential versus the amplitude A for the sets of parameters (α, β), for different values of the vibroimpact coefficient r (Fig. 6), for different values of C_1 [Fig. 7(a)], and for different values of C_2 [Fig. 7(b)]. For the free-colored noise self-sustained birhythmic vibroimpact system, i.e., D = 0, the shape of the pseudopotential shows the double well characterizing the

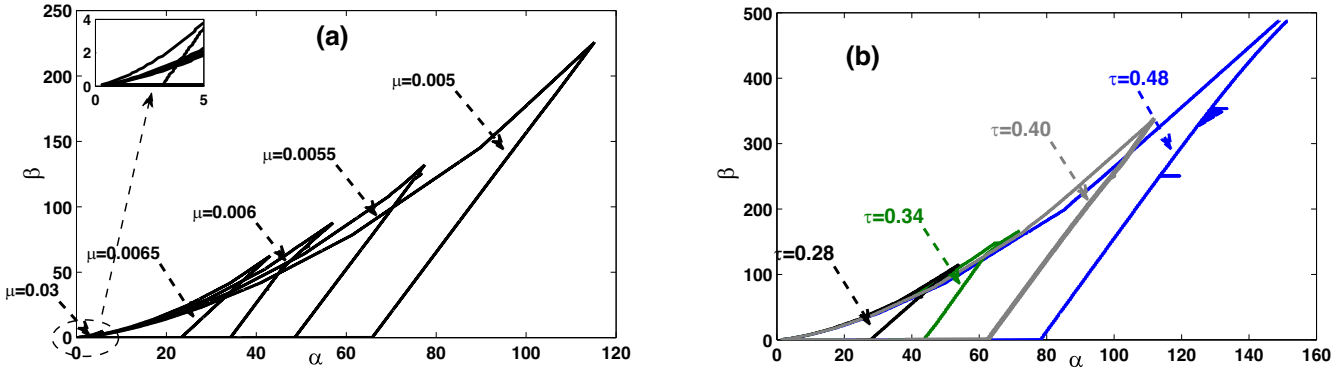


FIG. 4. Nonlinear parameter (a) (when $\tau = 0.12$) and correlation time (b) (when $\mu = 0.01$) effects on the domain of existence of three limit cycles in plane (α, β). Parameter values are $c_1 = 1.0$, $c_2 = -1.0$, $\omega_0 = 1.0$, $\zeta = -0.01$, $\lambda = 1.0$, $r = 0.95$, $D = 0.1$, $h = 0.0$, and $g = 1.0$.

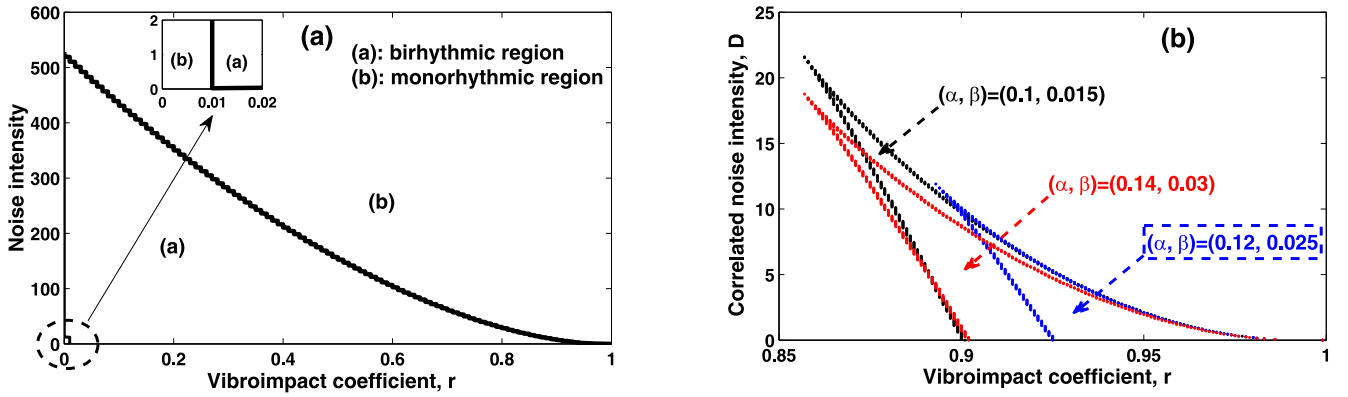


FIG. 5. Birhythmic zone in the parameter plane (r,D) when the control parameter is taken in the initial birhythmic zone (a) and when it is taken in the initial monorhythmic zone (b). Parameter values are $c_1 = 1.0$, $c_2 = -1.0$, $\omega_0 = 1.0$, $\zeta = -0.01$, $\lambda = 1.0$, $\mu = 0.01$, $\tau = 0.0001$, $h = 0.0$, and $g = 1.0$.

birhythmic behavior and for almost all control parameters (α, β), the depth of potential in A_3 is widely bigger that the one in A_1, meaning that for a variation of almost all the parameters of the system, it will be highly unlikely within the explored parameter range for this potential well to disappear. The depth of the well represents the system's stability, with a deeper well resulting in a more effective energy barrier. Increasing the vibroimpact coefficient, we discover that the two wells endure, despite the influence of r, for attractors $(\alpha, \beta) = (0.17, 0.0035)$, but the depth in A_1 disappears from a value of C_1 and C_2. However, stability is compromised as the wells go shallower.

B. Transition rate

1. *Vibroimpact and correlation time effect on escape time from the periodic attractors*

At nonzero-colored noise intensity ($D \neq 0.0$), because of the bistability of the potential present for a low setting value of the random force, two cases appear in Figs. 6 and 7. When the system is trapped at the minimum, the effective potential moves from left to right (or in the opposite direction) depending on the initial condition. During the escape, the vibroimpact system under colored noise excitation crosses the unstable limit-cycle amplitude A_2 (i.e., $|A| > A_2$, respectively, $|A| < A_2$) with an activation energy provided by the random force, which is equivalent to the depth of the left (respectively, right) well of the bistable potential.

Knowing the depth of the bistable potential's wells, the transition time from one well to the other is computed by taking the average of a series of times T_i required for the system to move from one attractor to another under the influence of correlated noise. For each series, the integration starts at $t = 0$, and the system is initialized in one well. Using the finite-difference approach with the time step, we estimate the time T_i by numerically integrating equation (15). The system's random movement caused by noise indicates that the transition or escape occurs with probability one in a finite amount of time. The inverse of Kramers' escape rate is the escape time expressed by the following expression:

$$T_i = \exp \frac{\Delta U_i}{D'}. \tag{25}$$

Thus, T_1 corresponds to the average transition time of the system from an attractor with limit-cycle amplitude A_1 to an attractor with limit-cycle amplitude A_3, and T_3 corresponds to the reverse case. For a set control parameter (α, β) taken in the birhythmic region in Fig. 1, we present in Fig. 8 the average escape time (on a logarithmic scale) as a function of

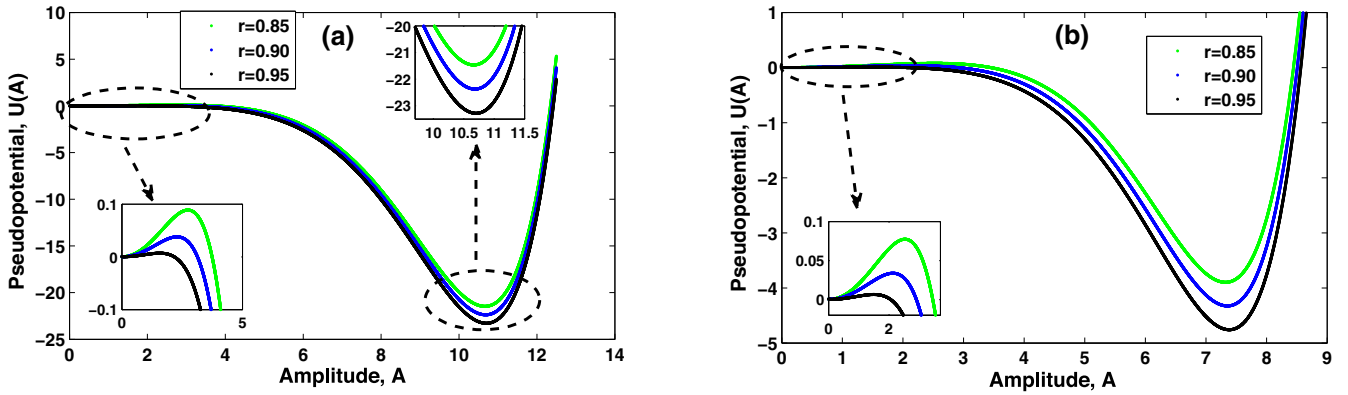


FIG. 6. Effects of the vibroimpact coefficient on the pseudopotential U(A), Eq. (17), for two different control parameters (α, β): $(\alpha, \beta) = (0.09, 0.001)$ (a) and $(\alpha, \beta) = (0.17, 0.0035)$ (b). The parameter values are $c_1 = 1.0$, $c_2 = -1.0$, $\omega_0 = 1.0$, $\zeta = -0.01$, $\lambda = 1.0$, $D = 0.02$, $\mu = 0.01$, $\tau = 0.1$, $h = 0.0$, and $g = 1.0$.

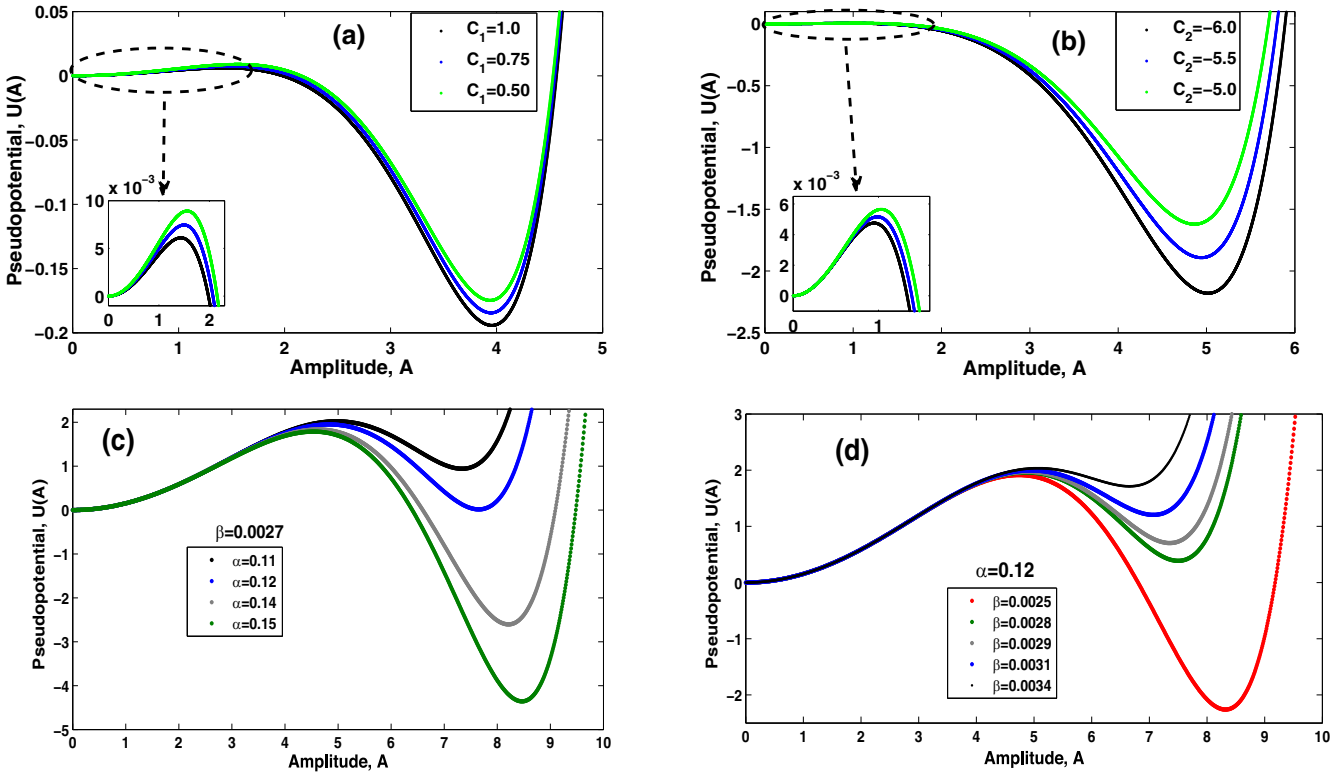


FIG. 7. Effects of the small power coefficient of Rayleigh damping variant C_1 when $C_2 = -1$ (a) and C_2 when $C_1 = -1.0$ (b) on the pseudopotential U(A), Eq. (17), for two different control parameters (α, β): $(\alpha, \beta) = (0.09, 0.01)$ (a) and $(\alpha, \beta) = (0.17, 0.0035)$ (b), and effects of control parameters α and β when $c_1 = 1.0, c_2 = -1.0$. The parameter values are $\omega_0 = 1.0, \zeta = -0.01, \lambda = 1.0, D = 0.02, \mu = 0.01, \tau = 0.1, r = 0.95, h = 0.0$, and $g = 1.0$.

the inverse of the correlated noise intensity D' for a low-noise strength and in the both transitions ($A_1 \to A_3$, $A_3 \to A_1$). It is observed that the logarithm of the average escape time obtained starting from simulations for the limit-cycle amplitudes A_1 and A_3 increases exponentially with the reverse of the intensity D of the correlated noise. With the parameter sets (α, β), we find that the variation of the average escape time strongly depends on the nonlinear coefficients and the vibroimpact coefficient and, for high values of correlation noise intensity, the depth of the well of potential with the limit-cycle A_1 decreases significantly, and the system will leave it quickly. For different values of the vibroimpact coefficient, the logarithmic average escape time from one attractor to another is not a linear function of the inverse correlated noise intensity.

2. Residence time

In Fig. 8, it is also observed that for large values of the intensity of the correlated noise, the system escapes quickly from the attractor with limit-cycle A_1.

Figure 6 does not show the duration of the system in a specific attractor. The average persistence time or residence time on the attractors is provided below. The vibroimpact system can spend short or extended periods of time in attractors with stable limit-cycle amplitudes A_1 or A_3, depending on the correlated noise intensity. For example, because the well in A_3 is deeper, the system spends considerably more time in the limit-cycle attractor A_3 due to the high energy barrier. The residence times Rs_1 and Rs_3 indicate the relative stabilities of attractors in A_1 and A_3, respectively. To measure the various escape times or transition times from one well to the other, we found the average persistence or residence time $Rs_{1,3}$ on the attractors with limit cycle amplitude $A_{1,3}$ as

$$Rs_1 = \sqrt{\frac{2\pi}{\ddot{U}(A_1)|\ddot{U}(A_2)|}}\exp\left(\frac{U(A_2)-U(A_1)}{D'}\right)$$
$$Rs_3 = \sqrt{\frac{2\pi}{\ddot{U}(A_3)|\ddot{U}(A_2)|}}\exp\left(\frac{U(A_2)-U(A_3)}{D'}\right). \quad (26)$$

This preamble helps to numerically verify the residence time analysis. In reality, the quantities Rs_i are both numerically accessible by direct simulations of the entire model equation (1) and analytically predicted by Eq. (17) via Eq. (26). Correlated noise can significantly alter the dynamics of a deterministic system. Figure 9 illustrates how correlated noise strength affects residence time. In this figure, we plot the residence time in both transitions, in both analytical (solid lines) and numerical (dashed lines), and we remark that for the set vibroimpact value, when correlated noise intensity increases, the residence time in the transition $A_1 - A_3$ decreases and the other one in the transition $A_3 - A_1$ increases. Regarding Fig. 9, it is important to note that the agreement between numerical and analytical results is fairly good in all the transitions. The combined effects of correlation time and vibroimpact coefficient on residence time are presented in Fig. 10. We confirm that for

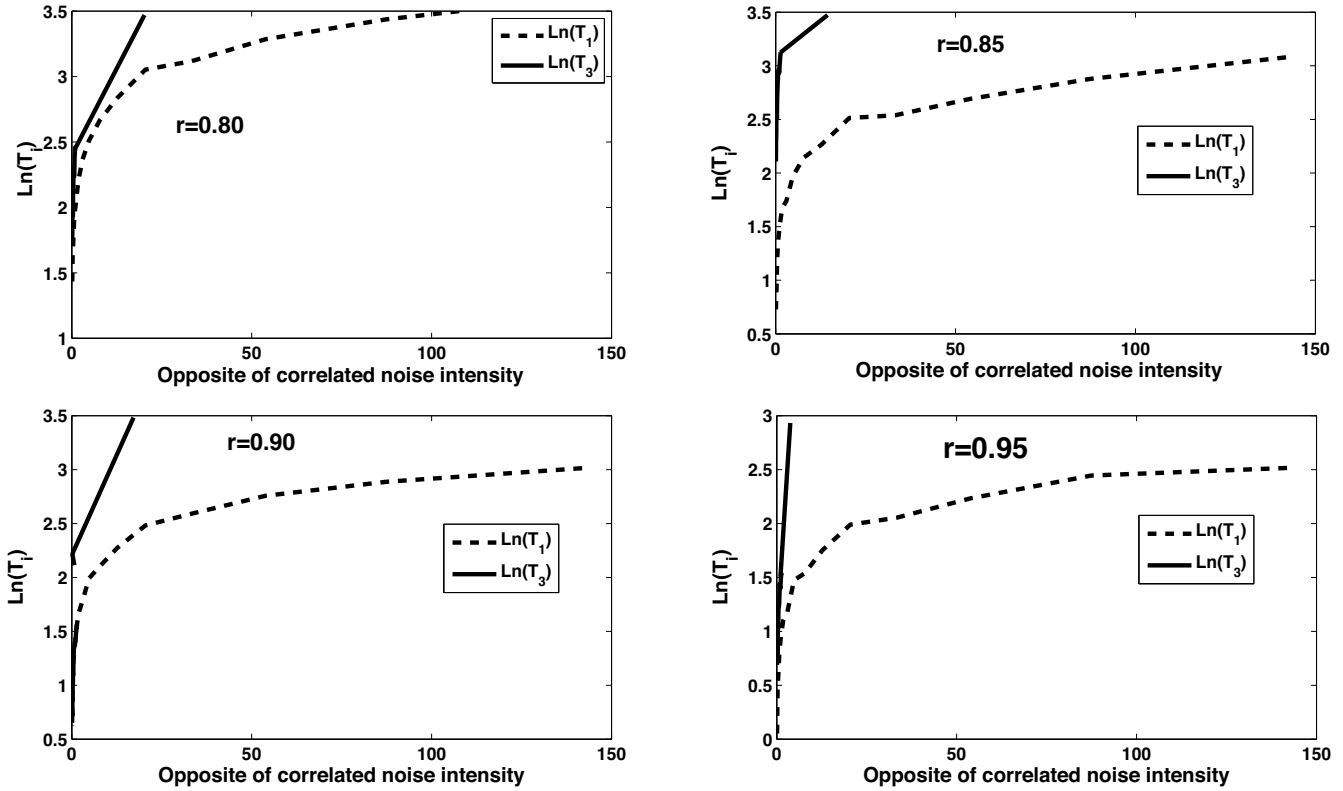


FIG. 8. Effect of the vibroimpact coefficient on the variation of the logarithmic average of the escape time from an attractor $A_1 \Leftrightarrow A_3$ versus $1/D$, for the sets of parameters $(\alpha, \beta) = (0.288, 0.0256)$. The solid line (T_3) refers to escape from the outer circle, while the dashed line (T_1) refers to the escapes from the inner circle. The parameter values are $c_1 = 1.0$, $c_2 = -1.0$, $\omega_0 = 1.0$, $\zeta = -0.01$, $\lambda = 1.0$, $\mu = 0.01$, $\tau = 0.4$, $h = 0.0$, and $g = 1.0$.

a vibroimpact system, the transition between the two opposite cases where one attractor is overwhelmingly dominant (i.e., a change of 2 orders of magnitude of the relative residence times) occurs within a very narrow change of the vibroimpact coefficient and correlated noise parameters. Stronger correlated noise supplies more energy to the system, helping it overcome pseudopotential barriers between attractors. This accelerates transitions and reduces residence times in one rhythm. Longer correlation durations indicate that noise disturbances remain, occasionally resonating with the oscillator's inherent frequency and encouraging escapes. Higher restitution coefficients reduce dissipation during hits, allowing the system to store more kinetic energy and switch rhythms more quickly.

3. Mean first passage time

A bistable system is a foundational theoretical model for understanding nonequilibrium phase transitions, which have many important properties in nonlinear stochastic systems. In this regard, a bistable gadget is technically based on research into the statistical features of a bistable model. The average first-passage time in bistable vibroimpact systems with weak damping caused by correlated noise excitations is investigated. The mean first-passage time can characterize a nonlinear vibroimpact system's transient behavior under correlated noise excitations. This study examines how correlation time, vibroimpact coefficient, and potential asymmetry affect mean first-passage time (MFPT) in an asymmetric bistable vibroimpact system with additive correlated noise at both crossings. Numerical results presented in Fig. 11 show how the correlation time and vibroimpact coefficient affect the MFPT in the same way; the coupling strength and asymmetry of the potential affect the MFPT in the same way. Increased correlation time improves the escape rate; however, increased vibroimpact diminishes the escape rate. So, for three values of vibroimpact, we plot the mean first passage time as a function of correlation time when noise intensity is 0.2.

4. Vibroimpact and correlated noise effects on energy barrier

In nonequilibrium vibroimpact systems without a bona fide potential, energy barriers are evaluated indirectly. After computing Kramers' escape time, Eq. (25) yields the maximum height of the potential barrier (energy of activation). The effective activation energy is determined by low-correlated noise intensity asymptotes; nevertheless, including high-correlated noise strength points (i.e., locations where the relationship is not linear) in the computing process can have an impact on the accuracy of numerical-simulation results. In the reverse interpretation of Kramers' reasoning, the effective activation energy is the slope of the logarithm of the escape time function of the reciprocal of the correlated noise intensity [27] for very low-correlated noise strengths. This approach uses the barrier of the effective potential $\Delta U_{1,3}$ to summarize system behavior during escape times. Indeed,

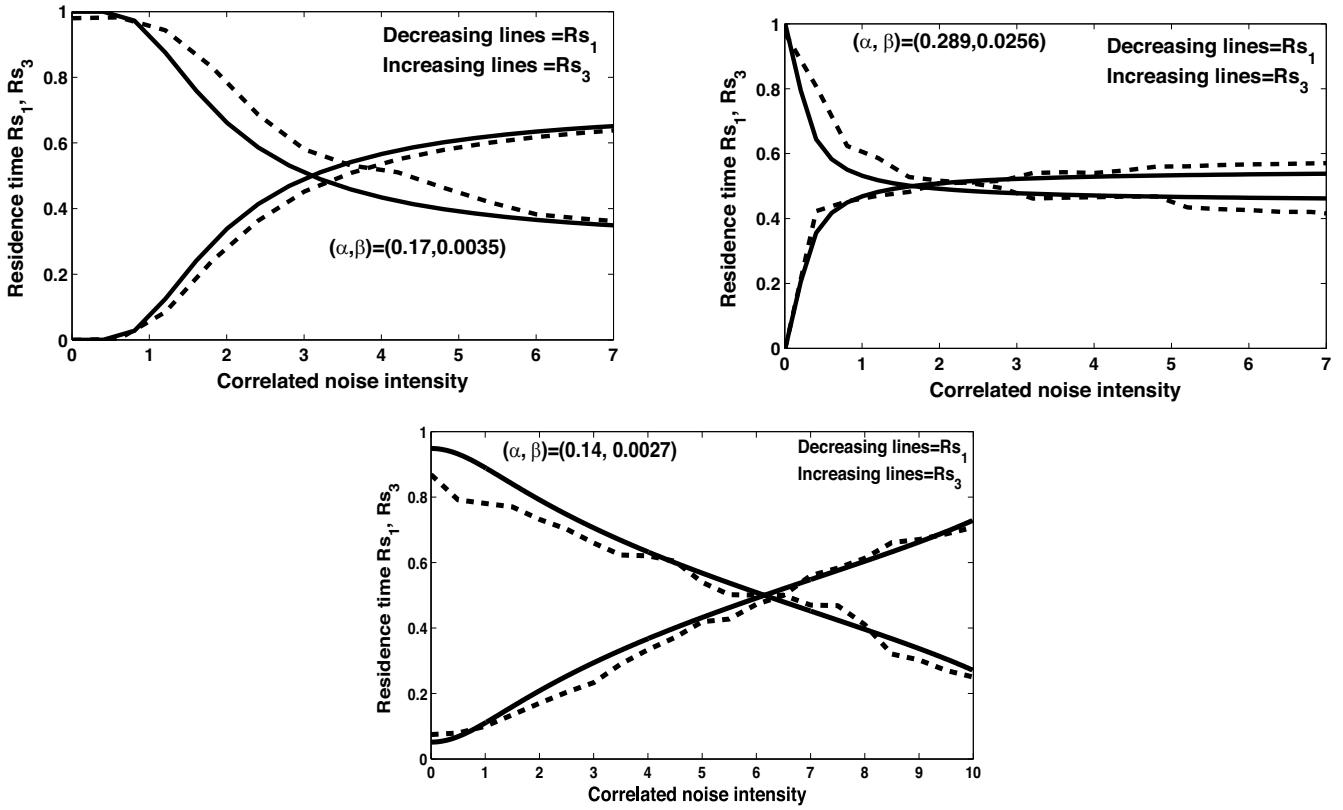


FIG. 9. Plot of residence times, analytic (solid lines), numerical (dashed lines) versus correlated noise intensity for two different values of the control parameter and in both transitions ($A_1 \to A_3$ and $A_3 \to A_1$). The parameter values are $c_1 = 1.0$, $c_2 = -1.0$, $\omega_0 = 1.0$, $\zeta = -0.01$, $\tau = 0.2$, $\lambda = 1.0$, $\mu = 0.01$, $r = 0.85$, $h = 0.0$, and $g = 0.0$.

by adapting a straight line through the data points in the linear part of Eq. (25) and measuring its slope (in Fig. 8), we obtain an evaluation of ΔU_1 and ΔU_3, the respective activation energies necessary for the system to escape from the attractor with limit cycles A_1 and A_3. Here, we collect the simulations of Eq. (1) with numerical simulations proposed in [26] to confirm the analytical results. We begin by investigating the low-noise behavior to check that the pseudopotential approximation is valid, as shown in Fig. 12. The numerical simulations have been performed to retrieve the escape rate, analogous to Eq. (26) from numerical simulations of Eq. (1). This prediction of the theoretical analysis, as summarized by Eq. (17), is confirmed in Fig. 12, where we plot numerical (dashed blue lines) and analytical (solid black lines) energy barriers ΔU_1 and ΔU_3 as a function of the vibroimpact coefficient [Fig. 12(a)] and correlation time [Figs. 12(b) and 12(c)]. When the effect of vibroimpact is presented, decreasing and increasing lines denote ΔU_1 and ΔU_3, respectively. When the influence of correlation time is displayed, growing and decreasing lines denote ΔU_1 and ΔU_3, respectively. We consistently observe a similar pattern for both analytical and numerical outcomes. Figure 13 illustrates the 3D plot of these energies.

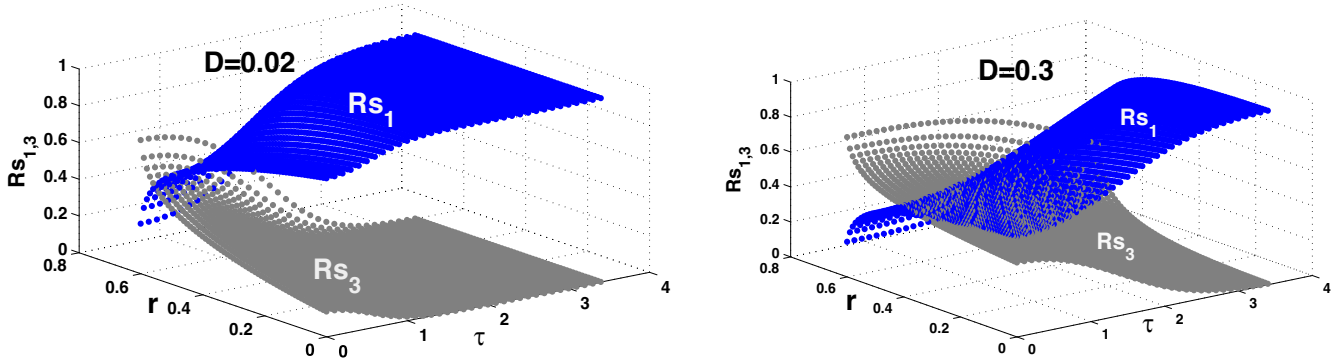


FIG. 10. Plot of 3D residence times versus correlation time and vibroimpact coefficient for two different values of correlated noise intensity and in the both transitions ($A_1 \to A_3$ and $A_3 \to A_1$). The parameter values are $c_1 = 1.0$, $c_2 = -1.0$, $\omega_0 = 1.0$, $\zeta = -0.01$, $\lambda = 1.0$, $\mu = 0.01$, $h = 0.0$, $(\alpha, \beta) = (0.288, 0.0256)$, and $g = 0.0$.

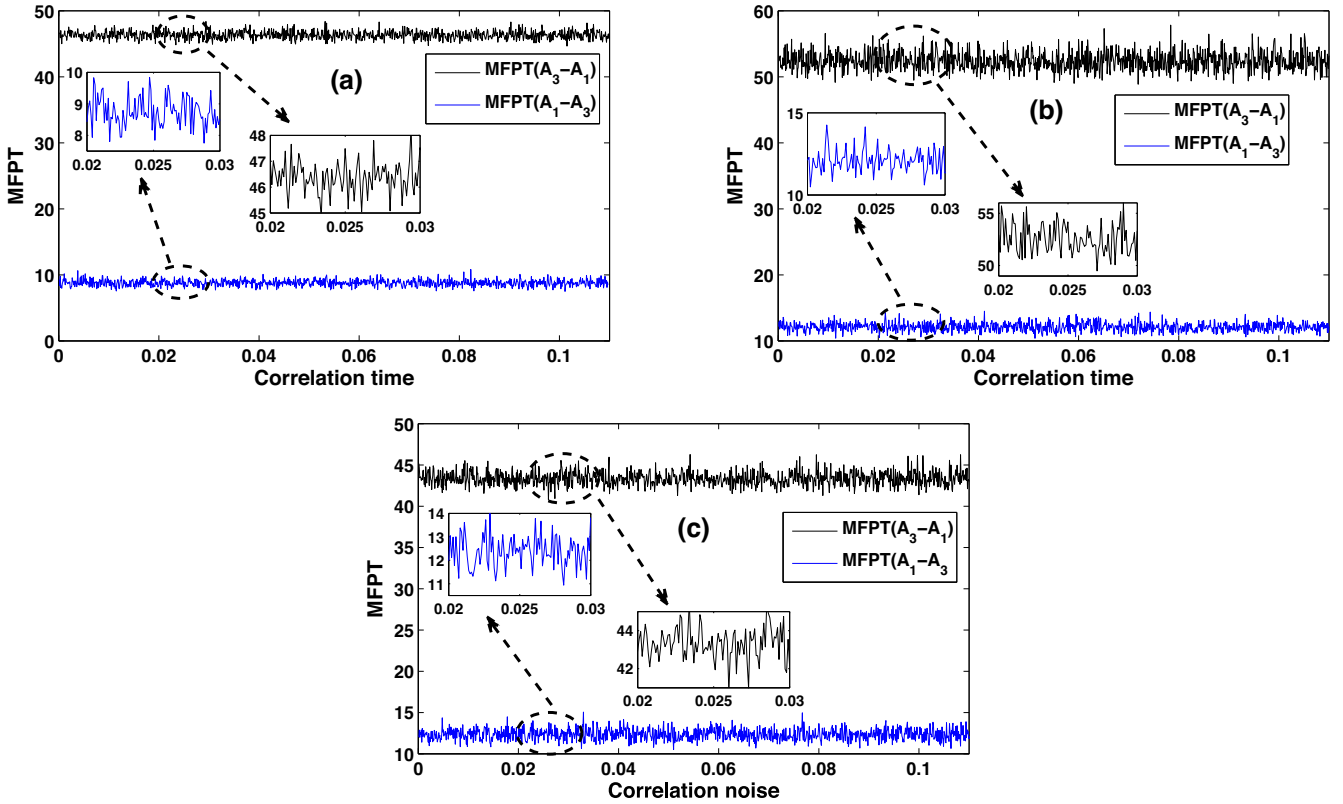


FIG. 11. Plot of mean first passage time (MFPT) versus noise correlation time in both transitions ($A_1 \to A_3$ and $A_3 \to A_1$ for some values of the vibroimpact coefficient [$r = 0.95$ (a), $r = 0.90$ (b), and $r = 0.85$ (c)]. The parameter values are $c_1 = 1.0$, $c_2 = -1.0$, $\omega_0 = 1.0$, $\zeta = -0.01$, $D = 0.2$, $\lambda = 1.0$, $\mu = 0.01$, $h = 0.0$, $(\alpha, \beta) = (0.288, 0.0256)$, and $g = 1.0$.

IV. RECURRENCE PLOTS QUANTIFICATION AND STOCHASTIC BIFURCATIONS: FOKKER-PLANCK EQUATION OF THE AVERAGED ORBIT PROBABILITY DISTRIBUTION

A. Correlation time and restitution effect on time series and recurrence analysis in self-sustained VI system

The techniques in this subsection are illustrated using data from numerical investigation of System 1 with the set parameters: $c_1 = 1.0$, $c_2 = -1.0$, $\omega_0 = 1.0$, $\zeta = -0.01$, $\lambda = 1.0$, $D = 0.08$, $h = 0.0$, and $g = 0.0$. Recurrence analysis in nonlinear systems for time series is based on the study of a matrix Re, whose members are defined as

$$\mathrm{Re}_{ij} = \begin{matrix} 1{:}\Phi_i \approx \Phi_j \\ 0{:}\Phi_i \neq \Phi_j \end{matrix} \quad i, j = 1 \ldots N, \tag{27}$$

where $\Phi(x, y)$ is the state vector, N is the length of the time series, i and j refer to the row and column of the matrix, respectively, and $\Phi_i \approx \Phi_j$ are equal to an error of ϵ. These indices also refer to time $t = i\Delta t$, where Δt is the sampling time. The elements of the matrix Re are determined by comparing the state of the system at time i,j, obtained with a threshold accuracy of ϵ. Thus, formally,

$$\mathrm{Re}_{ij} = \theta(\epsilon - \|\Phi_i - \Phi_j\|), \tag{28}$$

with $\|(.)\|$ being the Euclidean norm, and $\theta(\epsilon - \|\Phi_i - \Phi_j\|) = 1$ if $\epsilon > \|\Phi_i - \Phi_j\|$, $\theta(\epsilon - \|\Phi_i - \Phi_j\|) = 0$ if $\epsilon < \|\Phi_i - \Phi_j\|$ is the Heaviside function. The graph of the recurrence plot is obtained by plotting the Re_{ij} elements with different colors. By this definition, the recurrence plot diagram is always symmetric (i.e., $\mathrm{Re}_{ij} = \mathrm{Re}_{ji}$). Note that in data-based time series analysis, it is important to reconstruct the phase space of the system by estimating the corresponding time delays and the embedding dimension. This is the dimension of the homeomorphism of the actual (real) phase space in which the dynamics of the system are fully described. In this analysis, without loss of generality, it is assumed that the homeomorphism is the actual space itself. In other words, the embedding dimension is equal to 2 (which corresponds to the dimension of the state vector $\Phi(x, y)$), and the time delay between x and y can be determined from the average mutual information. It is important to emphasize that the choice of ϵ is important, and several techniques for selecting the appropriate value of ϵ have been developed in various research fields such as medicine, mechanics, and recurrence plot theories. In each case, the choice of the threshold recurrence ϵ is not unique, but it largely determines the analysis. A recurrence plot (RP) is a plot showing, for each time point j, the times at which the state of a dynamical system returns to its previous state at i, i.e., when the phase space trajectory visits approximately the same region of phase space as time j. In simpler terms, it is a plot of $\vec{x}(i) \approx \vec{x}(j)$, showing i on a horizontal axis and j on a vertical axis, where $\vec{x}$ is the state of the system (or its phase space trajectory). By using the RPs technique on our system, we discovered that the basin of attraction in Fig. 3 can also be derived by calculating the probability of recurrence (one of the well-known recurrence

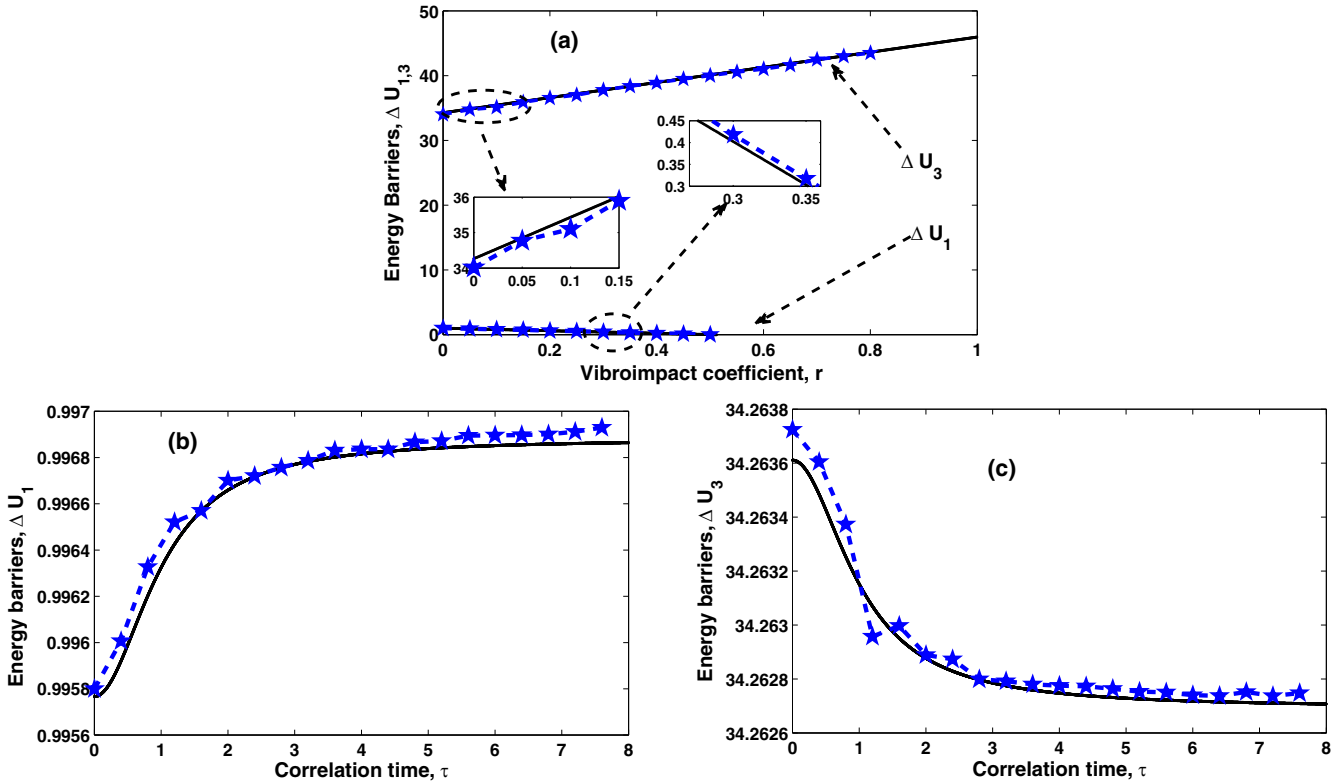


FIG. 12. Comparison of analytical [as per Eq. (19), solid black lines] and numerical [as per Eq. (4), dashed blue lines] energy barriers as a function of the vibroimpact coefficient [panel (a) when $\tau = 0.1$ and $D = 0.0001$] and noise correlation time [panels (b) and (c) when $r = 0.95$ and $D = 0.2$]. The parameters of the system are: $(\alpha, \beta) = (0.09, 0.001)$, $c_1 = 1.0$, $c_2 = -1.0$, $\omega_0 = 1.0$, $\zeta = -0.01$, $\lambda = 1.0$, $\mu = 0.01$, $h = 0.0$, and $g = 1.0$.

quantification analysis parameters [28]), which may be utilized to identify the domains

$$RR_{\tau_0} = \frac{1}{N - \tau_0} \sum_{i=0}^{N-\tau_0} R_{i,i+\tau_0}(\epsilon), \tag{29}$$

where τ_0 is the set time and N is the total number of points in the phase space. Our goal here is to provide an estimate of the possibility that the system returns to its prior structure after time τ_0, also known as the τ_0-recurrence rate. To justify the choice of embedding and threshold, three checks are performed in Fig. 14 for a representative case in the birhythmic regime for $(\alpha, \beta) = (0.144, 0.005)$ and $r = 0.99$. First, the delay τ_0 is selected as the first local minimum of the average mutual information (AMI) between $x(t)$ and $x(t + \tau_0)$ [29]. This minimum occurs at $\tau_0 = 1.16$ time units as shown in Fig. 14(a). Second, the embedding dimension is verified using the false nearest-neighbors (FNN) algorithm of Kennel *et al.* [30]. The fraction of false neighbors falls from 94.4 percent at $m = 1$ to 0.0 percent at $m = 2$ and remains negligible for $m \geqslant 2$ [Fig. 14(b)], confirming that a two-dimensional embedding is sufficient and consistent with the dimension

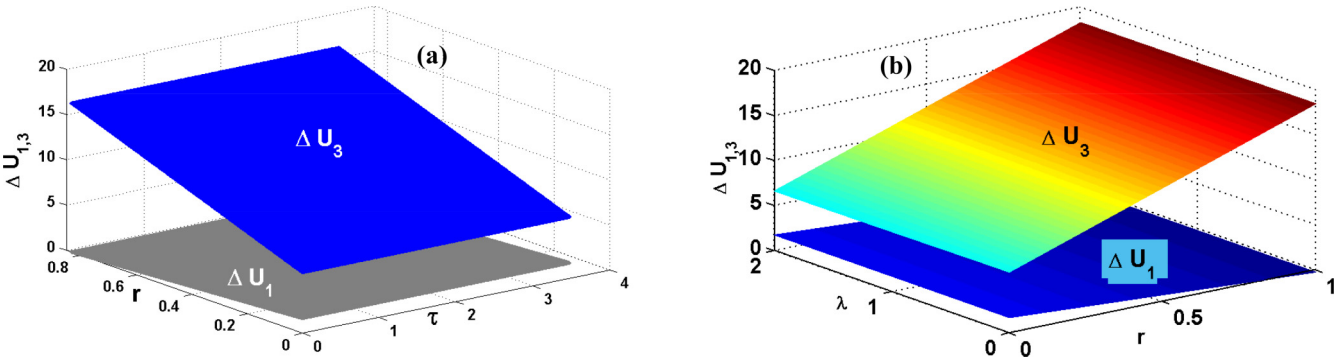


FIG. 13. Plot of energy barriers in three dimensions as a function of the vibroimpact coefficient and correlation time [panel (a) when $\lambda = 0.1$] and noise vibroimpact coefficient and λ [panel (b) when $\tau = 0.1$]. The parameters of the system are: $(\alpha, \beta) = (0.09, 0.001)$, $c_1 = 1.0$, $c_2 = -1.0$, $\omega_0 = 1.0$, $\zeta = -0.01$, $D = 0.2$, $\mu = 0.01$, $h = 0.0$, and $g = 1.0$.

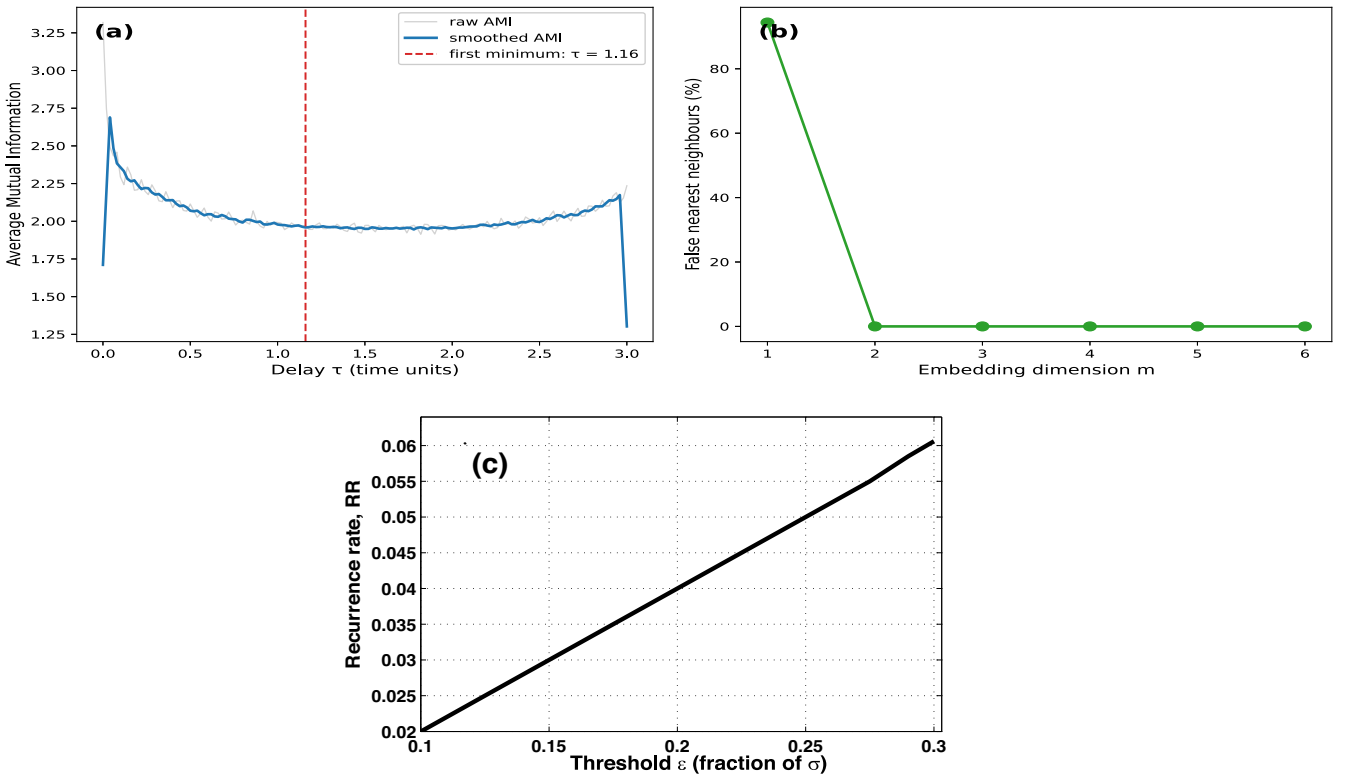


FIG. 14. Embedding and threshold justification. (a): average mutual information (AMI) versus delay, (b): false nearest-neighbors (FNN) versus embedding dimension and (c): recurrence rate (RR) versus threshold for $(\alpha, \beta) = (0.144, 0.005)$, $c_1 = 1.0$, $c_2 = -1.0$, $\omega_0 = 1.0$, $\lambda = 0.1$, $\tau = 0.1$ $\zeta = -0.01$, $D = 0.0000001$, $\mu = 0.01$, $r = 0.99$ $h = 0.0$, and $g = 1.0$.

of the physical state vector $\Phi(x, \dot{x})$. Although the full state vector $\Phi(x, \dot{x})$ is available from the numerical integration of Eq. (1), the recurrence and mutual information analysis of this section is carried out on the delay-reconstructed vector $\Phi_{\tau_0}(t) = [x(t), x(t + \tau_0)]$, so that the method remains applicable to a single observable (as would be the case for experimental time series). Third, the sensitivity of the recurrence quantification to the threshold ϵ is tested over the range $\epsilon \in (0.10, 0.15, 0.20, 0.25, 0.30)\sigma$ where σ is the standard deviation of the reconstructed trajectory following the fixed number of neighbors recommendation of Marwan *et al.* [28]. As shown in Fig. 14(c), the recurrence rate varies smoothly with ϵ ($RR = 0.023$ at 0.10σ to $RR = 0.070$ at 0.30σ), with no discontinuity indicative of a qualitative change in recurrence structure over this range. We therefore retain $\epsilon = 0.2$ for consistency with the pseudopotential and escape-time analysis of Sec. III, noting that this choice lies within a stable region of the (ϵ, RR) relationship.

Two representative time series for four exemplary values of the restitution coefficient are shown in Fig. 15(a_1). The figure shows the results of two initial conditions, namely, one around the origin, $(x_0, \dot{x}_0) = (0.1, 0.1)$ (to target the small-amplitude LC) represented by the black line, and another far from the origin, $(x_0, \dot{x}_0) = (6.0, 6.0)$ (to target the large-amplitude LC) represented by the blue lines. The time series plots for different values of the restitution coefficient clearly depict the presence of birhythmicity in the VI model. The recurrence rate (RR) is the most straightforward indicator of RQA, whose definition is $\frac{1}{N^2}\sum R_{i,j}$, which corresponds to the chance that a state would repeat. Illustration of the system free response is shown in Fig. 15 for the parameters of Fig. 3 for $(\alpha, \beta) = (0.144, 0.005)$, $r = 0.99$ [Figs. 15(a_1)–15(c_1)], $r = 0.97$ [Figs. 15(a_2)–15(c_2)], $r = 0.95$ [Figs. 15(a_3)–15(c_3)], and $r = 0.93$ [Figs. 15(a_4)–15(c_4)]. In Figs. 15(b_1) and 15(c_1), the RPs of both initial conditions are indiscernible. The graphs corresponding to the initial condition $(x_0, y_0) = (0.1, 0.1)$ are presented in Fig. 15(b_1), while those for the initial conditions $(x_0, y_0) = (6.0, 6.0)$ are shown in Fig. 15(c_1), and we note that, as with limit cycles, RPs are also very sensitive to initial conditions. States of nonlinearity can be determined using a recurrence analysis method on a time series data collection, and by deciphering some quantification characteristics of a given data, the condition of occurrence in the future may be established. In the absence of correlated noise, Fig. 16 shows how the self-sustained vibroimpact system's recurrence rate varies with the restitution coefficient. The recurrence rate indicates the likelihood that the system will return to a previously visited state after a specific time, providing information about the stability and predictability of oscillatory dynamics. A higher restitution coefficient (closer to elastic impact) indicates lower energy loss during collisions. This permits the system to maintain oscillations with a larger frequency, resulting in higher repetition rates. This figure demonstrates that, in the absence of external stochastic forcing, the restitution coefficient can regulate the degree of regularity in the system's dynamics. Vibroimpact dissipation shapes recurrence parameters and determines whether the system exhibits strong birhythmic behavior or wanders towards irregular oscillations. Lower restitution coefficients, on the other hand, cause greater dissipation at

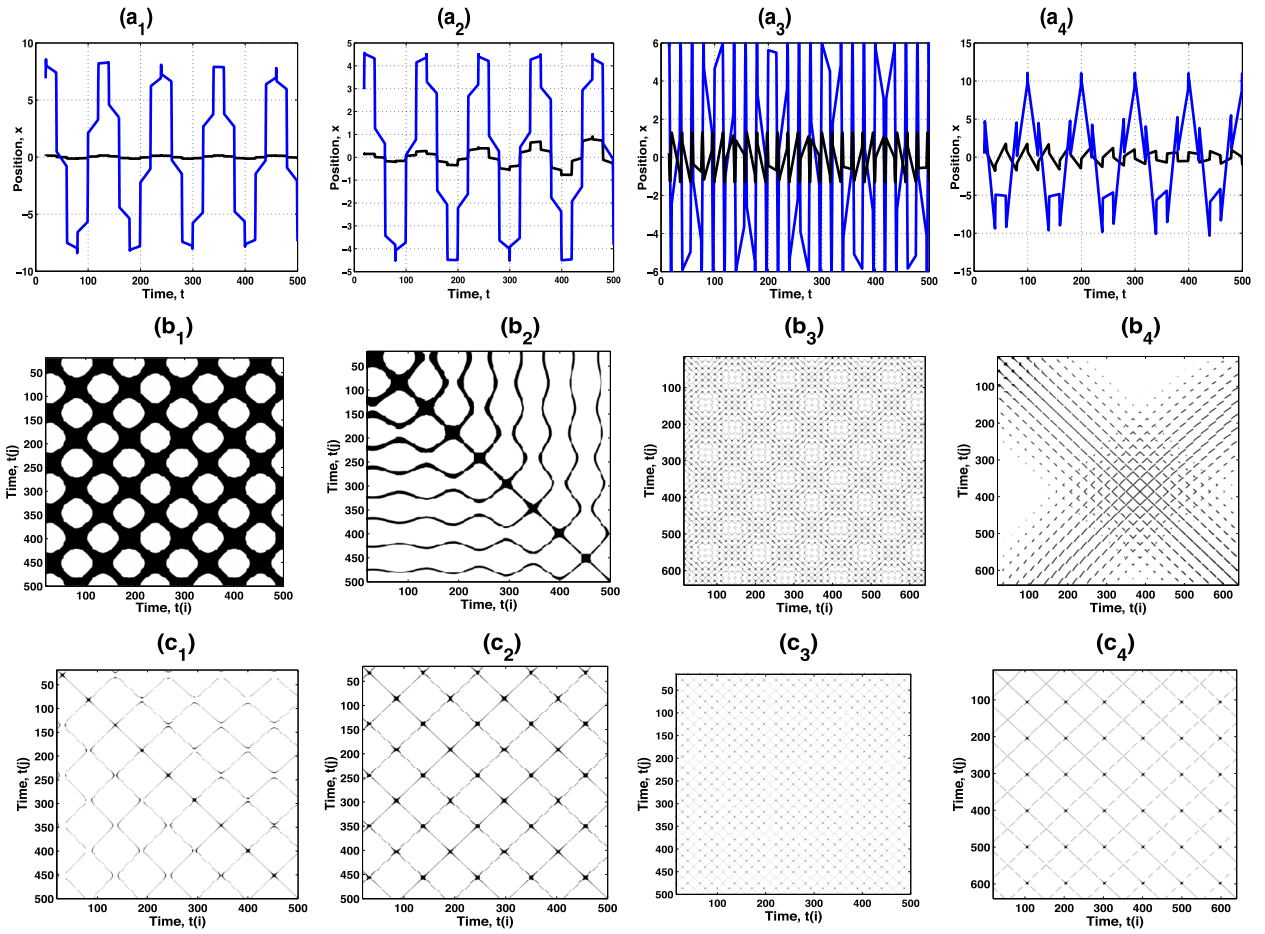


FIG. 15. Response of the vibroimpact system for $(\alpha, \beta) = (0.144, 0.005)$, $c_1 = 1.0$, $c_2 = -1.0$, $\omega_0 = 1.0$, $\zeta = -0.01$, $\lambda = 1.0$, $D = 0.0$. (a_1): Time series plots when the initial condition is taken near the inner orbit (blue curve) and the other orbit (black curve) when $r = 0.99$ (a_1), $r = 0.95$ (a_2), r = 0.92 (a_3), and $r = 0.90$ (a_4). (b_1) and (c_1) correspond to the recurrence plots of the vibroimpact system when the initial condition is taken respectively near the first orbit and near the second orbit with $r = 0.99$ (b_1 and c_1), $r = 0.95$ (b_2 and c_2), $r = 0.92$ (b_3, c_3), and $r = 0.90$ (b_4, c_4).

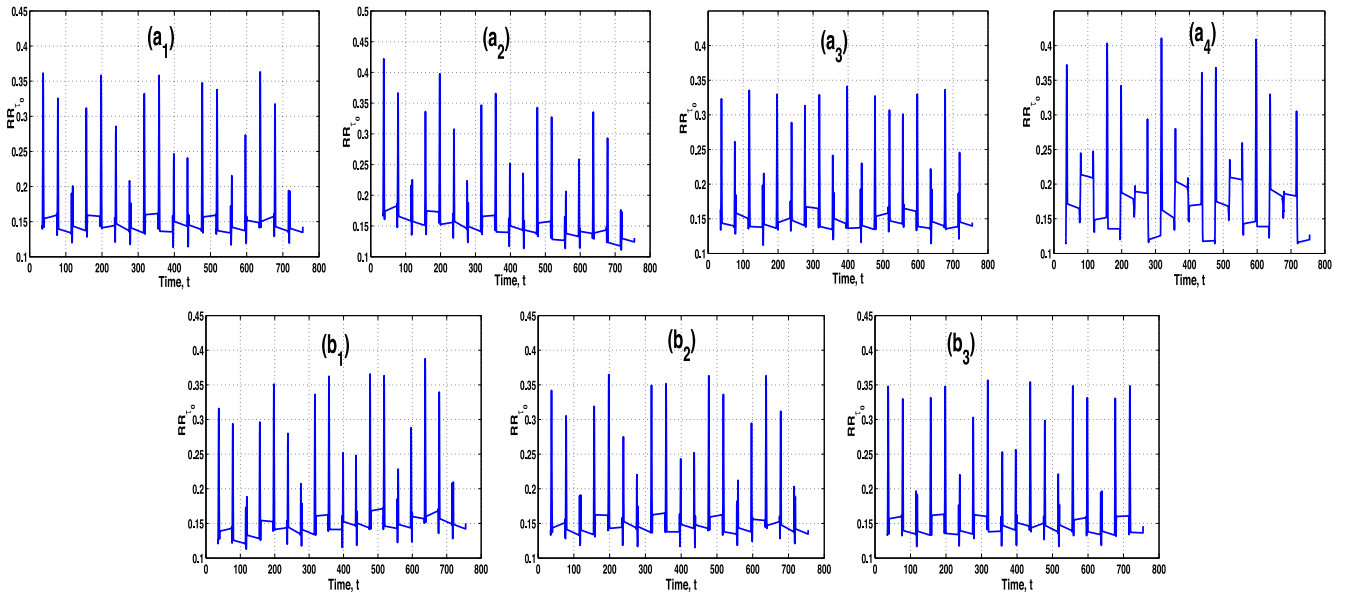


FIG. 16. Probability of recurrence after a very short time τ_0 (τ_0-recurrence rate) for the self-sustained system for different values of the restitution coefficient without correlated noise: with $r = 0.99$ (a_1 and b_1), $r = 0.95$ (a_2 and b_2), $r = 0.95$ (a_3, b_3), and $r = 0.90$ (a_4). The other parameter values are: $c_1 = 1.0$, $c_2 = -1.0$, $\omega_0 = 1.0$, $\zeta = -0.01$, $\lambda = 1.0$, $\beta = 0.04$, $\alpha = 0.17$, $h = 0.0$, $g = 0.0$, and $\mu = 0.01$.

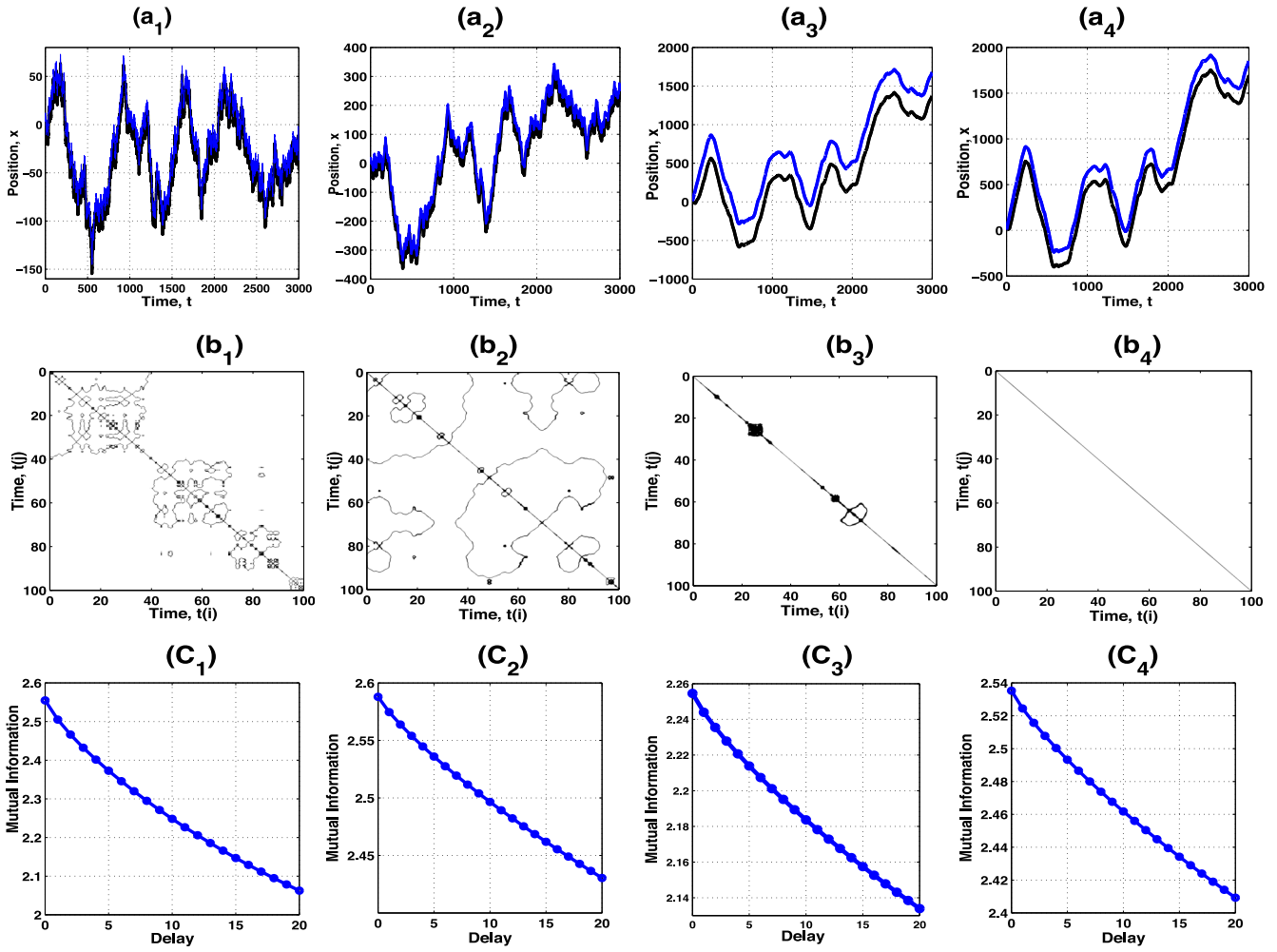


FIG. 17. Time series of different transitions, recurrence plots, and mutual information versus delay for different values of correlation time: $(a_1, b_1, c_1) \mapsto \tau = 0.00001$, $(a_2, b_2, c_2) \mapsto \tau = 0.001$, $(a_3, b_3, c_3) \mapsto \tau = 0.1$, and $(a_4, b_4, c_4) \mapsto \tau = 0.5$. The other parameter values are: $c_1 = 1.0$, $c_2 = -1.0$, $\omega_0 = 1.0$, $\zeta = -0.01$, $\lambda = 1.0$, $r = 0.95$, $\beta = 0.04$, $\alpha = 0.17$, $D = 0.08$, $h = 0.0$, $g = 0.0$, and $\mu = 0.01$.

impacts, disrupting periodicity and decreasing the likelihood of recurrence. Without correlated noise, recurrence behavior is essentially determined by the balance of self-sustaining Rayleigh energy input and dissipation during strikes. When energy loss is small ($r \cong 1.0$), trajectories are restricted to stable limit cycles, resulting in numerous recurrences. When energy loss is substantial ($r < 1.0$), trajectories deviate more strongly, lowering repetition rates and indicating diminished rhythmic stability.

In Fig. 17(a_1), in the both initial conditions (blue line for the small-amplitude LC) and (black line for the large-amplitude LC), a sequence of discrete-time data points, which is listed in order of time, is plotted for four different values of noise correlation time. We can observe that when the correlated noise intensity is 0.08, for a very small value of correlation time, the time series is almost the same for the both initial conditions and starts to be different when $\tau > 0.04$. Then, the influence of the correlation time on the RPs is presented in Fig. 17(b_1) for a fixed value of the noise intensity. Based on the qualitative change in correlation time, the behavior of a trajectory of a dynamic system in phase space. The correlation time governs how long random fluctuations remain coherent before decorrelating, and it has a direct impact on the system's ability to switch between attractors. Mutual information, in brief, measures the amount of data that we acquire by measuring one random variable against another. Interestingly, very short delay times provide near-linear reconstructions with substantial correlations between consecutive phase space points, but extremely lengthy delays may obfuscate the deterministic structure that connects points along a single degree of freedom. If the delay period corresponds to a characteristic time in the underlying dynamics, the reconstruction process may also be affected. The mutual information between two attractors versus time delay is plotted in Fig. 17(c_1), and it is shown that for all values of the correlation time, this mutual information decreases when the delay time increases. For a delay of 20 ms, for example, the mutual information is 1.8076, 2.0342, 2.1086, and 2.4081, respectively, for $\tau = 0.00001$, 0.001, 0.1, and 0.5. When noise is nearly white (extremely short correlation), the perturbations are fast and unstructured. The system receives regular little kicks, but these are ineffective at facilitating transitions across possible barriers. As a result, the time series exhibits prolonged residence in one attractor with fewer changes. Finally, quantifying

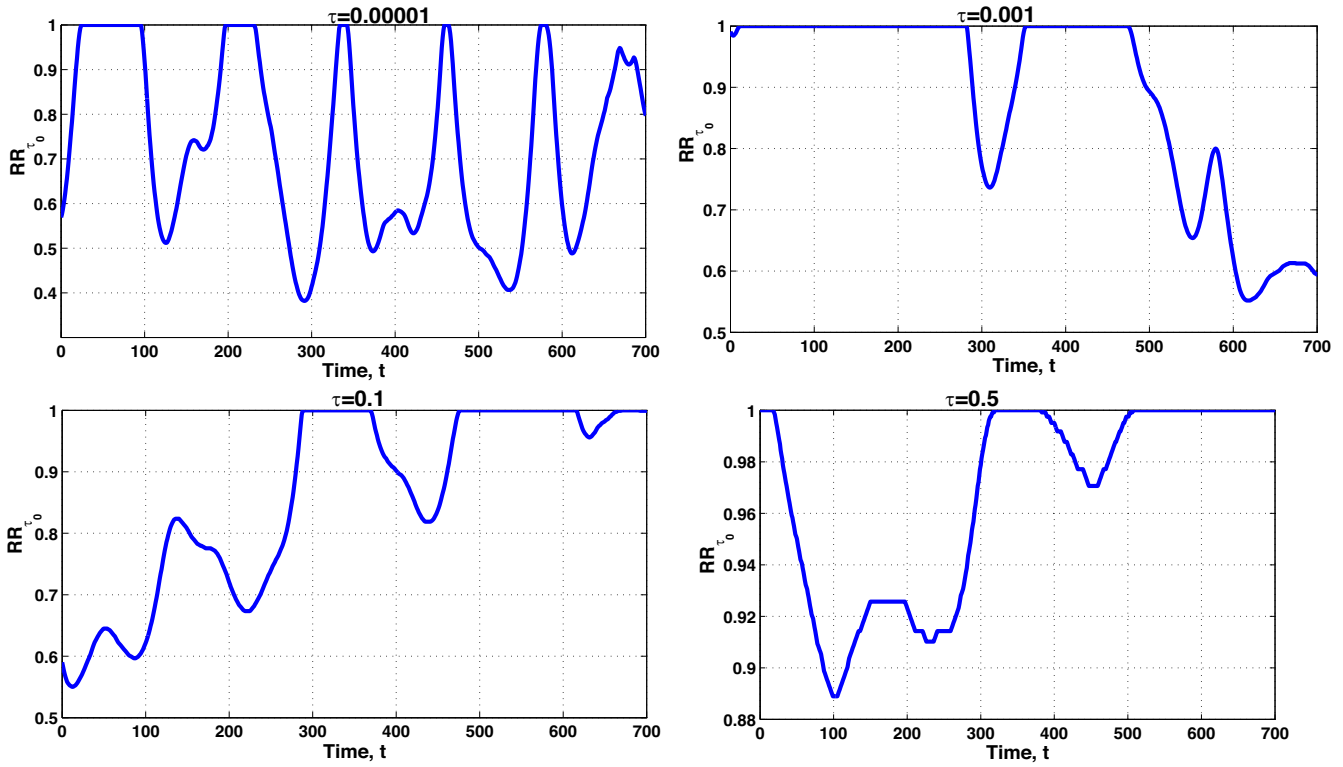


FIG. 18. Probability of recurrence after time τ_0 (τ_0-recurrence rate) for the self-sustained system for different values of the correlation time. The other parameter values are: $c_1 = 1.0$, $c_2 = -1.0$, $\omega_0 = 1.0$, $\zeta = -0.01$, $\lambda = 1.0$, $r = 0.95$, $\beta = 0.04$, $\alpha = 0.17$, $D = 0.08$, $h = 0.0$, $g = 0.0$, and $\mu = 0.01$.

the dynamics of the multirhythmic Rayleigh system using recurrence plots provides a handy way to compare even the hidden recurrence aspects of their dynamics. Figure 18 shows the effect of noise correlation time on recurrence rate. These dynamics were highly variable since they were discovered to be quite sensitive to variations in correlation time and restitution coefficient, which explains their importance in adapting vibroimpact systems to external inputs. The correlation time essentially adjusts the memory of the stochastic force. Short memory (low correlation) creates frenetic but ineffective perturbations, whereas long memory (high correlation) generates organized disturbances that can either reinforce or destabilize rhythmic states. This explains why the quantity, timing, and regularity of transitions in the time series are substantially dependent on correlation time. These figures show that not only noise strength but also its temporal structure (correlation time) are important in determining birhythmic transitions. It demonstrates how correlated noise can operate as a rhythm-switching regulator, providing a technique for tuning stability in engineering systems and understanding rhythm variability in biological oscillators. These findings demonstrate that recurrence plots are an effective diagnostic tool for detecting birhythmic and multirhythmic regimes. They present quantitative evidence that vibroimpact dissipation and associated noise are major controllers of rhythm changeover. In practice, tuning restitution coefficients and noise parameters allows one to intentionally regulate the predictability, stability, and variability of oscillatory activity in engineering and biological systems.

B. Stochastic bifurcations: Fokker-Planck equation of the averaged orbit probability distribution

A higher correlated noise intensity increases the probability density of amplitude and the likelihood of stochastic bifurcation caused by control parameters [26,27]. In this section, various degrees of control parameters, the restitution coefficient, which represents the degree of energy loss of the system when an impact happens, and noise correlation time are studied to ensure the dependability and precision of the suggested approach. The suggested method's accuracy was verified by comparing the analytical stationary probability density to numerical results from the original system (1). Several techniques and algorithms exist to solve stochastic differential equations [27], including the implicit midpoint rule with Heun and Leapfrog approaches, as well as quicker numerical algorithms like the stochastic version of the Runge-Kutta approaches and a quasisymplectic algorithm [17,26,27]. The Box-Muller approach generates exponentially correlated noise-distributed random variables from Gaussian white noise and two uniformly distributed random numbers on a particular interval, as outlined in [17]. When $c_1 = 1.0$, $c_2 = -1.0$, $\omega_0 = 1.0$, $\zeta = -0.01$, $\mu = 0.01$, $h = 0.0$, and $g = 1.0$ are fixed, all stationary probability of amplitude A for different correlation times, control parameters [shown in subcaptions (i)–(iii)] and nonlinear parameters are shown respectively in Figs. 19 and 20. By fixing the correlation time, the vibroimpact coefficient, and the nonlinear parameter, an interesting revival and collapse of multirhythmicity with variation of correlation time

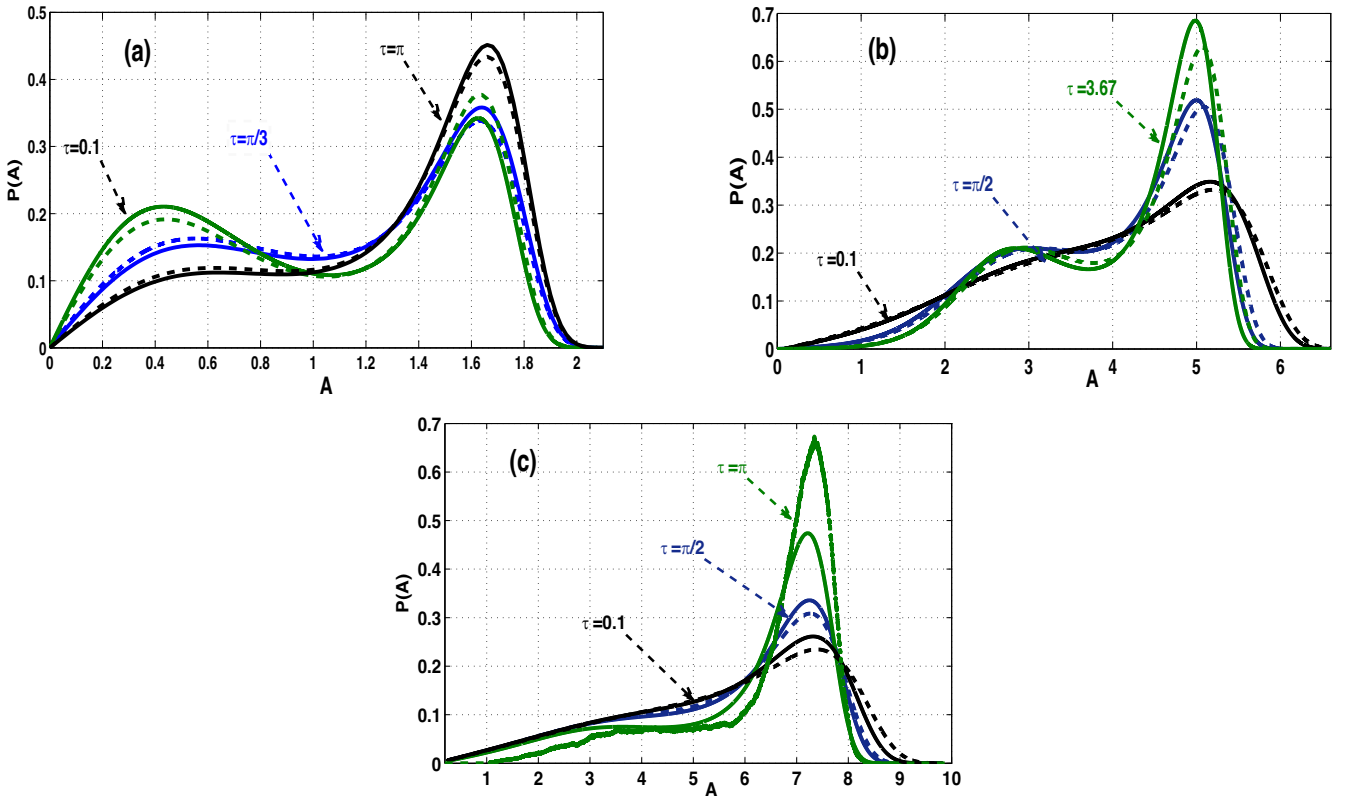


FIG. 19. Probability distributions of the amplitude for different values of control parameters $[(\alpha, \beta) = (0.255, 0.0184)$ (a), $(\alpha, \beta) = (0.17, 0.004)$ (b), and $(\alpha, \beta) = (0.12, 0.0032)$ (c)] and for different correlation times when the correlated noise intensity is $D = 0.7$. Solid lines denote the analytical results, while dashed lines denote numerical results. The parameters of the system refer to: $c_1 = 1.0$, $c_2 = -1.0$, $\omega_0 = 1.0$, $\zeta = -0.01$, $\lambda = 1.0$, $\mu = 0.01$, $r = 0.95$ $h = 0.0$, and $g = 1.0$.

and nonlinear parameter can be detected in Figs. 19 and 20, respectively. In these figures, the comparison between the analytical result (solid lines) and the Monte Carlo simulation (dots) is done, and good agreement between these two simulations is observed. These figures indicate that the influence of noise correlation time and the nonlinear parameter on the response of the vibroimpact system (1) exists. For $\tau(\mu) = 0.1(0.00025)$, $\frac{\pi}{2}$ (0.1), the amplitude distribution is, respectively, unimodal and bimodal when $(\alpha, \beta) = (0.17, 0.004)$. With a gradual increase of system parameters, the peaks of the PDF change considerably, and when the correlation time is taken in the b-rhythmic region, for example, the bifurcation has a different behavior (see the case where $\tau = 0.1$ and π in Fig. 19(a). Concretely, the increase of noise intensity D leads to the reduction of all stationary PDFs of amplitude, displacement, and velocity. Figures 21, 22, 23 and 24 show the effects of the system parameters on the joint probability.

V. CONCLUSION

This research investigates the steady-state behavior and bifurcation of a nonlinear vibroimpact multirhythmic extended Rayleigh system with friction generated by actual correlated noise. The nonsmooth transformation simplifies the vibroimpact self-sustaining system without obstacles, facilitating the extraction of theoretical results from it. The transformation transforms a nonsmooth system into a smooth multirhythmic system with low damping, modest noise intensities, small friction amplitudes, and restitution coefficients near unity. Stationary probability density functions are found using stochastic averaging. The PDF distribution of the impact multirhythmic system is further investigated in detail, taking into account parameters such as excitation intensity, control variables, correlation time, and restitution value. The proposed methods' analytical results are confirmed through comparison with the original nonlinear systems' simulated results. Analyzing the stationary response allows exploration of the stochastic P-bifurcation. The impact of the system parameter on energy barriers, escape time, residence time, and first passage time is explained. The combined probability density functions show that the interaction between friction amplitude and restitution coefficient can trigger the occurrence of stochastic P-bifurcation. Hence, by examining the crucial transition behavior of the system in this research, we can uncover when and how the Rayleigh damping variation, random noise, enhanced memory damping, and restitution coefficient of nonsmooth constraint act as the tipping point to indicate the desired dynamic motion of the multirhythmic oscillator. This helps in comprehending different real mechanical vibration processes. In addition to pseudopotential analysis, escape times, MFPT, and recurrence analysis are developed to provide a complementary perspective on system dynamics. Recurrence plots analyze the temporal structure

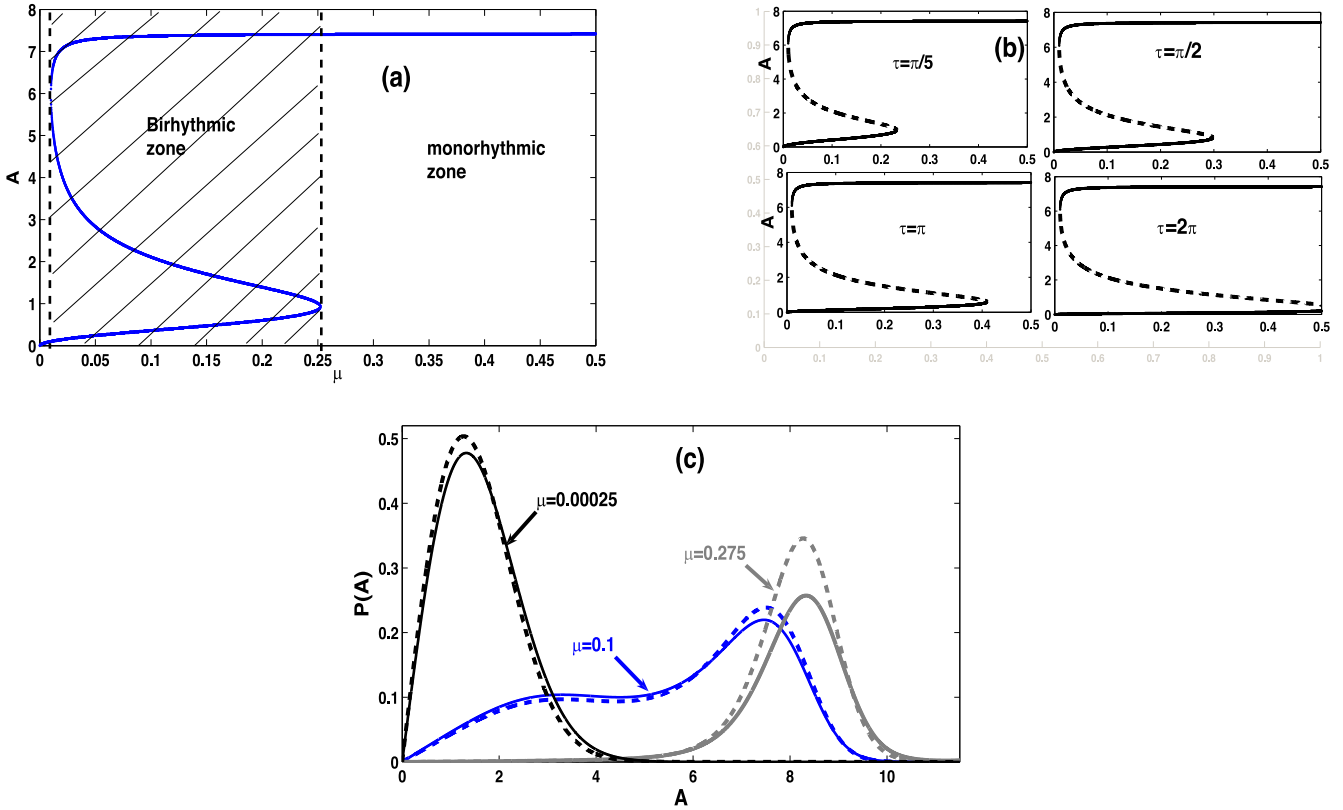


FIG. 20. (a) and (b): Amplitude versus nonlinear parameter for different values of correlation time. (c): analytical (solid lines) and numerical (dashed lines) of probability distributions versus amplitude for different values of nonlinear parameter when $\tau = 0.2$. The set parameters are: $(\alpha, \beta) = (0.17, 0.004)$, $c_1 = 1.0$, $c_2 = -1.0$, $\omega_0 = 1.0$, $\zeta = -0.01$, $r = 0.95$, $h = 0.0$, and $g = 1.0$.

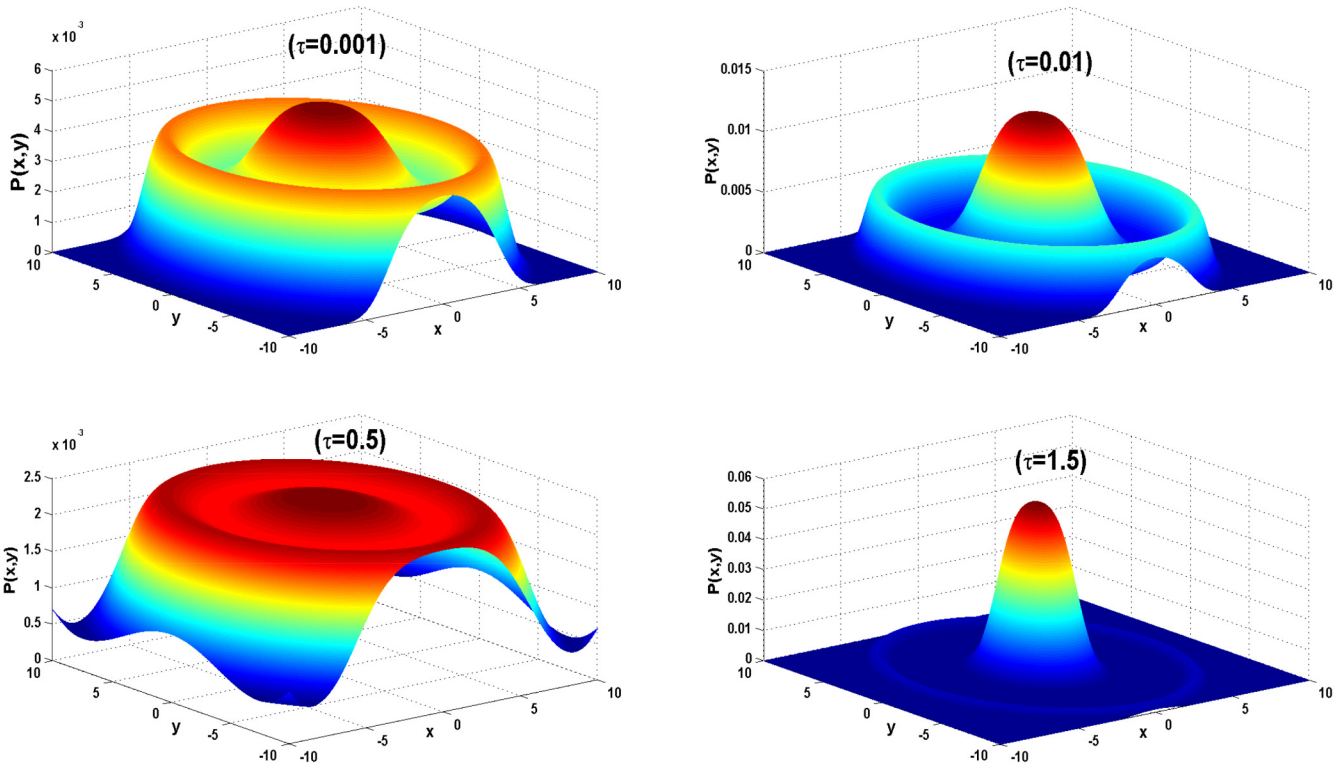


FIG. 21. Effect of correlation time on the joint probability, for $(\alpha, \beta) = (0.17, 0.004)$, $c_1 = 1.0$, $c_2 = -1.0$, $D = 0.7$ $\omega_0 = 1.0$, $\zeta = -0.01$, $\mu = 0.01$, $h = 0.0$, and $g = 1.0$.

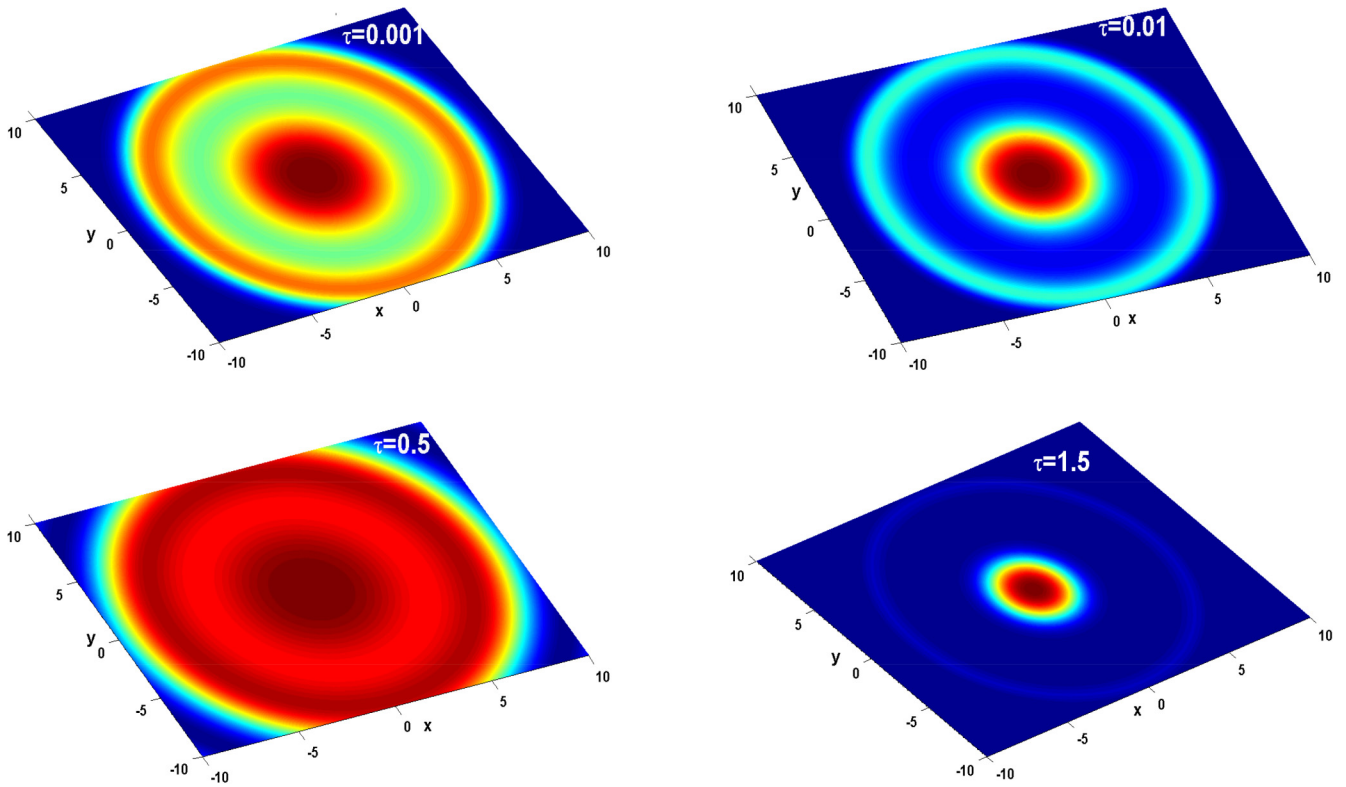


FIG. 22. Effect of correlation time on the joint probability, for $(\alpha, \beta) = (0.17, 0.004)$, $c_1 = 1.0$, $c_2 = -1.0$, $D = 0.7$ $\omega_0 = 1.0$, $\zeta = -0.01$, $\mu = 0.01$, $h = 0.0$, and $g = 1.0$.

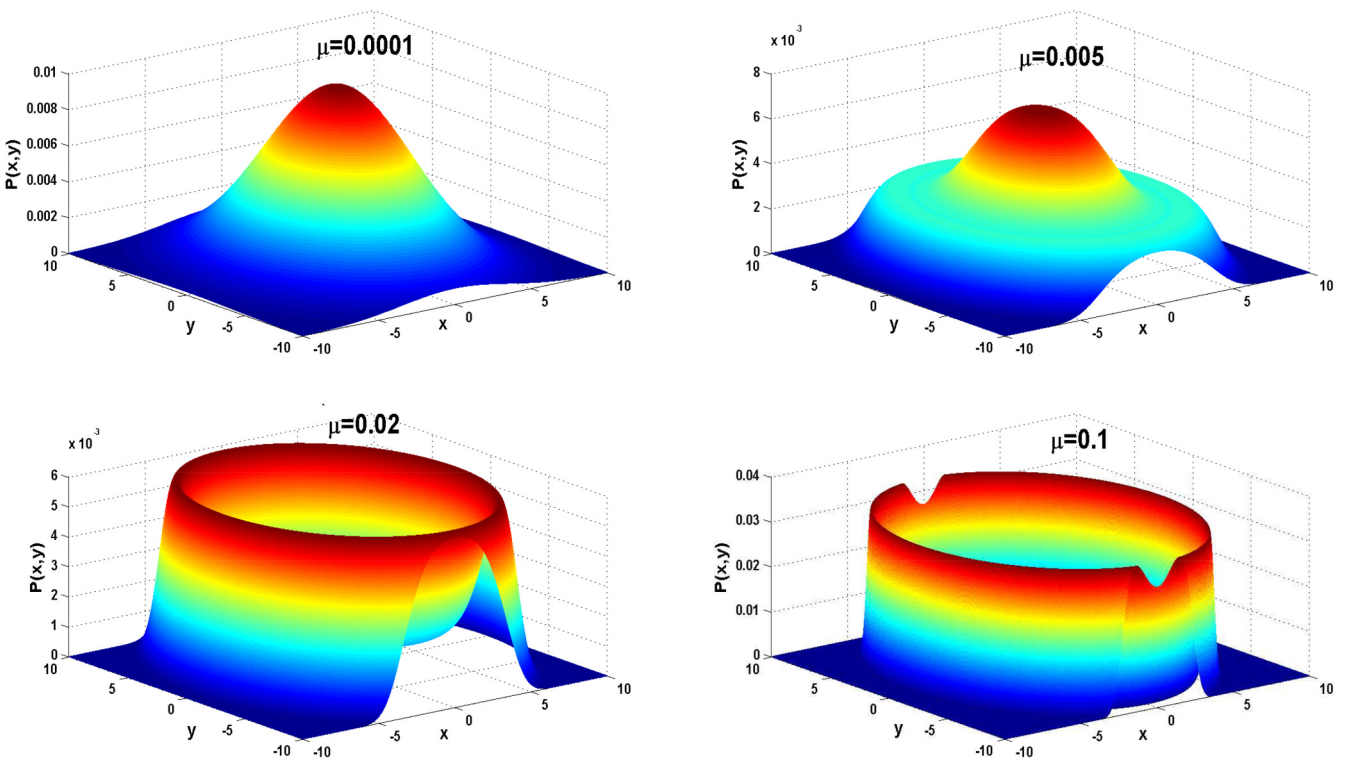


FIG. 23. Effect of nonlinear parameter μ on the joint probability, for $(\alpha, \beta) = (0.17, 0.004)$, $c_1 = 1.0$, $c_2 = -1.0$, $D = 0.7$ $\omega_0 = 1.0$, $\zeta = -0.01$, $\tau = 0.12$, $h = 0.0$, and $g = 1.0$.

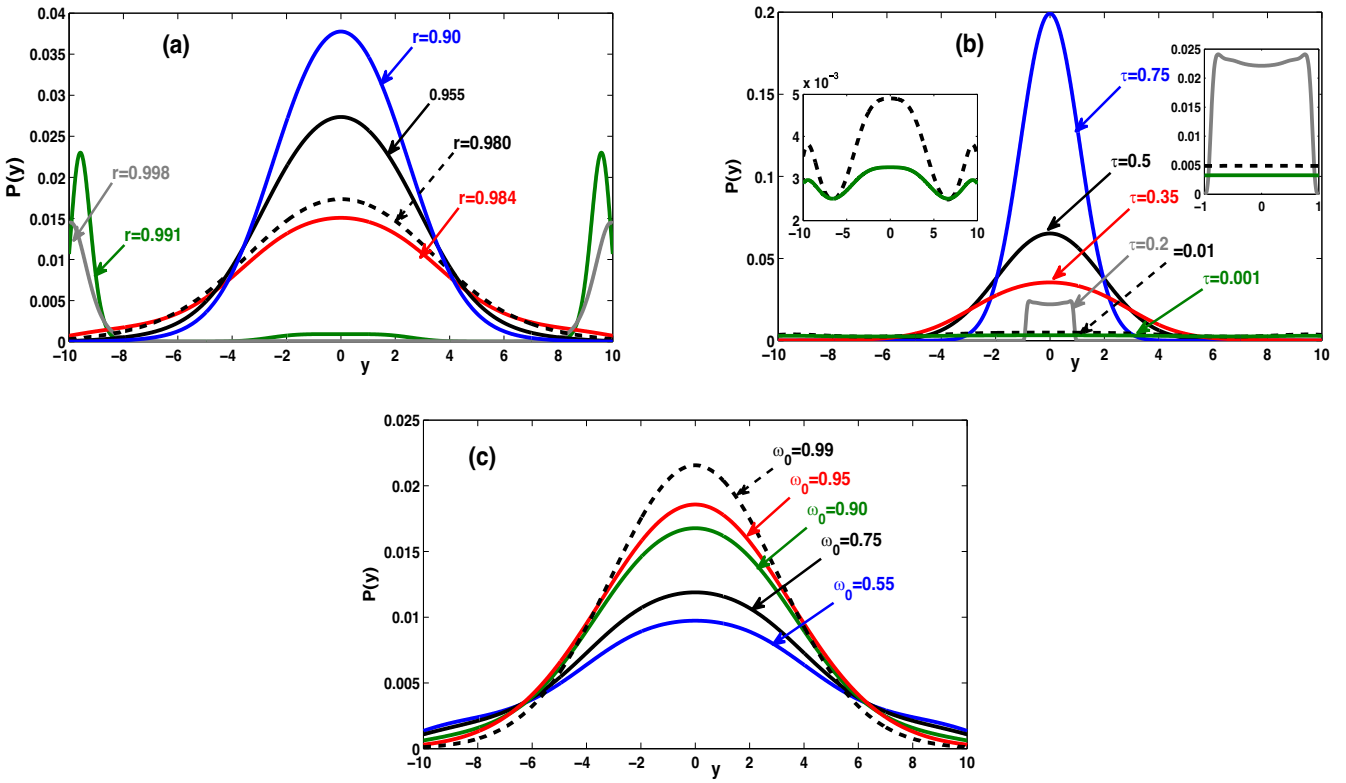


FIG. 24. Effects of the vibroimpact coefficient (when $\tau = 0.12$ and $\omega_0 = 1.0$), noise correlation time (when $r = 0.98$ and $\omega_0 = 1.0$) and frequency (when $r = 0.98$ and $\tau = 0.12$) on the joint probability in two dimensions, for $(\alpha, \beta) = (0.17, 0.004)$, $c_1 = 1.0$, $c_2 = -1.0$, $D = 0.7$, $\zeta = -0.01$, $h = 0.0$, and $g = 1.0$.

of oscillations in time series data, while energy-based approaches measure transitions between attractors. Quantifying recurrence rates and determinism can reveal minor changes in stability and predictability that potential-based techniques can not capture. Recurrence analysis is especially useful for systems with correlated noise and nonsmooth effects where trajectories are irregular and standard measurements may not adequately convey the complexity. Furthermore, we demonstrated that stable orbits can lead to two coexisting attractors in the presence of an external correlated noise stimulus, and that noise and restitution coefficient have a significant influence on recurrence rate quantification. Low recurrence rates are associated with poorer stability, as anticipated by pseudopotential analysis, but variations in determinism are associated with escape time distribution.

ACKNOWLEDGMENTS

R.M.Y. undertook this work with the support of the German Academic Exchange Service (DAAD), Germany. He acknowledges the support of the Potsdam Institute for Climate Impact Research (PIK), Potsdam, Germany.

The authors declare that they have no conflict of interest with publication of this work.

DATA AVAILABILITY

There are no publicly available research data or software supporting this manuscript. Requests for further information or data should be sent to the authors.

APPENDIX

In this Appendix, we extend the demonstration of Eq. (9),

$$\begin{aligned}\mathrm{sgn}(V_1)Z[\mathrm{sgn}(V_1)V_1+\Delta,\mathrm{sgn}(V_1)V_2] &= \int_0^t \zeta\exp[(t'-t)/\lambda](gA(t')\cos(\tilde{\omega}t'+\theta)\\ &\quad+\mathrm{sgn}[A(t')\cos(\tilde{\omega}t'+\theta)]g\Delta-h\tilde{\omega}A(t')\sin(\tilde{\omega}t'+\theta))dt'\\ &= \int_0^t dt'(g\zeta\cos(\tilde{\omega}t')e^{-t'/\lambda}V_1+h\zeta\cos(\tilde{\omega}t')e^{-t'/\lambda}V_2\\ &\quad+\tilde{\omega}h\zeta\sin(\tilde{\omega}t')e^{-t'/\lambda}V_1-\tilde{\omega}^{-1}g\zeta\sin(\tilde{\omega}t')e^{-t'/\lambda}V_2\\ &\quad+\mathrm{sgn}(A(t-t')\cos(\tilde{\omega}(t-t')+\theta))g\Delta e^{-t'/\lambda})\end{aligned}$$

$$
\begin{aligned}
&= \lambda(\tilde{\omega}^2\lambda^2+1)^{-1}\zeta([e^{-t/\lambda}(\tilde{\omega}\lambda\sin(\tilde{\omega}t)-\cos(\tilde{\omega}t)+\Lambda_1(\Delta))\\
&\quad +1]gV_1+[\lambda\tilde{\omega}^2-e^{-t/\lambda}(\tilde{\omega}\sin(\tilde{\omega}t)+\lambda\tilde{\omega}^2\cos(\tilde{\omega}t))]hV_1\\
&\quad +[1-e^{-t/\lambda}(\cos(\tilde{\omega}t)-\lambda\tilde{\omega}\sin(\tilde{\omega}t))]hV_2\\
&\quad +[e^{-t/\lambda}(\lambda\cos(\tilde{\omega}t)+\tilde{\omega}^{-1}\sin(\tilde{\omega}t)+\Lambda_2(\Delta))-\lambda]gV_2). \qquad \text{(A1)}
\end{aligned}
$$

[1] S. L. T. de Souza, A. M. Batista, I. L. Caldas, R. L. Viana, and T. Kapitaniak, Noise-induced basin hopping in a vibro-impact system, Chaos Solit. Fract. **32**, 758 (2007).

[2] C.-P. Tsai and W.-C. Li, Micromechanical vibro-impact systems: A review, J. Micromech. Microeng. **33**, 093001 (2023).

[3] Edited by R. A. Ibrahim, V. I. Babitsky, and M. Okuma, *Vibro-Impact Dynamics of Ocean Systems and Related Problems* (Springer, Berlin, Heidelberg, 2009), Vol. 44.

[4] Y. Yang, J. Wang, G. Zhu, W. Yang, and Q. Zhou, A thermomechanical model for mesh deflection calculation of crown spur gear pair, Meccanica **55**, 1393 (2020).

[5] H. Rong, X. Wang, W. Xu, and T. Fang, Resonant response of a non-linear vibro-impact system to combined deterministic harmonic and random excitations, Int. J. Non Linear Mech. **45**, 474 (2010).

[6] W. Goldsmith, *Impact: The Theory and Physical Behavior of Colliding Solids* (Edward Arnold, London, 1960).

[7] Z. L. Huang, Z. H. Liu, and W. Q. Zhu, Stationary response of multi-degree-of-freedom vibro-impact systems under white noise excitations, J. Sound Vib. **275**, 223 (2004).

[8] M. F. Dimentberg and A. I. Menyailov, Response of a single-mass vibroimpact system to white-noise random excitation, Z. Angew. Math. Mech. **59**, 709 (1979).

[9] A. P. Ivanov, Dynamics of systems with mechanical impacts, Moscow, International Education Program, Moscow **1997**, 113 (1997).

[10] V. I. Babitsky, *Theory of Vibroimpact Systems* (Nauka, Moscow, 1978).

[11] M. F. Dimentberg and D. V. Iourtchenko, Random vibrations with impacts: A review, Nonlinear Dyn. **36**, 229 (2004).

[12] M. Wiercigroch, Modelling of dynamical systems with motion dependent discontinuities, Chaos Solit. Fract. **11**, 2429 (2000).

[13] M. A. Savi, S. Divenyi, L. F. P. Franca, and H. I. Weber, Numerical and experimental investigations of the nonlinear dynamics and chaos in non-smooth systems, J. Sound Vib. **301**, 59 (2007).

[14] M. Elmegård, B. Krauskopf, H. M. Osinga, J. Starke, and J. J. Thomsen, Bifurcation analysis of a smoothed model of a forced impacting beam and comparison with an experiment, Nonlinear Dyn. **77**, 951 (2014).

[15] A. Zakharova, T. Vadivasova, V. Anishchenko, A. Koseska, and J. Kurths, Stochastic bifurcations and coherencelike resonance in a self-sustained bistable noisy oscillator, Phys. Rev. E **81**, 011106 (2010).

[16] N. Berglund and B. Gentz, On the noise-induced passage through an unstable periodic orbit II: General case, SIAM J. Math. Anal. **46**, 310 (2014).

[17] R. M. Yonkeu, R. Yamapi, G. Filatrella, and C. Tchawoua, Pseudopotential of birhythmic van der Pol-type systems with correlated noise, Nonlinear Dyn. **84**, 627 (2015).

[18] D. Wang, H. Pei, W. Xu, J. Yao, F. Hellmann, and J. Kurths, Transitions in a noisy birhythmic vibro-impact oscillator with improved memory damping regime, Nonlinear Dyn. **108**, 1045 (2022).

[19] A. Ivanov, Impact oscillations: Linear theory of stability and bifurcations, J. Sound Vib. **178**, 361 (1994).

[20] J. Qian and L. Chen, Random vibration of SDOF vibro-impact oscillators with restitution factor related to velocity under wide-band noise excitations, Mech. Syst. Sig. Process. **147**, 107082 (2021).

[21] J. Feng, W. Xu, and R. Wang, Stochastic responses of vibro-impact Duffing oscillator excited by additive Gaussian noise, J. Sound Vib. **309**, 730 (2008).

[22] D. Liu, M. Li, and J. Li, Probabilistic response and analysis for a vibro-impact system driven by real noise, Nonlinear Dyn. **91**, 1261 (2018).

[23] Y. G. Yang, Y. H. Sun, and W. Xu, Stochastic bifurcations of a fractional-order vibro-impact system driven by additive and multiplicative Gaussian white noises, Complexity, Hindawi **2019**, 1 (2019).

[24] P. Kumar, S. Narayanan, and S. Gupta, Stochastic bifurcations in a vibro-impact Duffing-Van der Pol oscillator, Nonlinear Dyn. **85**, 439 (2016).

[25] H. T. Zhu, Stochastic response of a vibro-impact Duffing system under external Poisson impulses, Nonlinear Dyn. **82**, 1001 (2015).

[26] R. M. Yonkeu, R. Yamapi, G. Filatrella, and C. Tchawoua, Stochastic bifurcations induced by correlated noise in a birhythmic van der Pol system, Commun. Nonlinear Sci. Numer. Simul. **33**, 70 (2016).

[27] R. M. Yonkeu, R. Yamapi, G. Filatrella, and C. Tchawoua, Effects of a periodic drive and correlated noise on birhythmic van der Pol systems, Physica A **466**, 552 (2017).

[28] N. Marwan, M. Carmenromano, M. Thiel, and J. Kurths, Recurrence plots for the analysis of complex systems, Phys. Rep. **438**, 237 (2007).

[29] A. M. Fraser and H. L. Swinney, Independent coordinates for strange attractors from mutual information, Phys. Rev. A **33**, 1134 (1986).

[30] M. B. Kennel, R. Brown, and H. D. I. Abarbanel, Determining embedding dimension for phase-space reconstruction using a geometrical construction, Phys. Rev. A **45**, 3403 (1992).